Conceptual Design of the XFEL Photoinjector

M. Ferrario (INFN-LNF), K. Flöttmann (DESY),
B. Grigoryan (YerPhI), T. Limberg (DESY),
Ph. Piot (DESY)

February 20, 2001

Abstract In this report the conceptual design for the TESLA X-ray free-electron laser photoinjector is presented. Beam Dynamics, design and operational issues are addressed.

Contents

1 Introduction

Accelerators for free-electron lasers (FELs) require high brightness electron beams (typically sub mrad mm transverse emittances, ps bunch length and nC charge per bunch). Since the beam quality can only degrade as the beam propagates along the accelerator up to the undulator, the demands on the injector performance are very challenging. In the TESLA XFEL, the required beam parameters are: transverse slice emittance of 1.6 mrad mm[1] (over a slice length of the order of the cooperation length) and a peak current of 5 kA at the undulator entrance. The injector proposed hereafter incorporates a photoemission radio-frequency (RF) gun, capable of producing a high bunch charge which is coupled to an accelerating section and a magnetic bunch compression section. Downstream of the bunch compressor, a matching and diagnostics section follows prior to subsequent acceleration in a chain of accelerator modules (the pre-accelerator).
In the second chapter of this report, an optimization of a photoinjector which results in the proposed design is presented. The effects of small perturbations on the initial conditions are studied to simulate drift and jitter of various sub-systems in Chapter 3. The fourth chapter describes the diagnostics section and measurement procedures.

2 Beam Dynamics Issues

2.1 Simulation Tools

The numerical simulations presented in this report have been performed using several computer codes. Because of the large parameter space that needs to be studied, the fast, multi-slice envelope code HOMDYN [1] has been used for parameters scans. The code is based on a semi-analytical approach of the dynamics of space charge dominated beams. The basic assumption is that the bunch can be described as a an array of uniformly charged cylinders of constant thermal emittance set to zero for the results presented in this report (multi-slice approximation). The length and radius of the bunch can vary under the effect of internal space charge forces and external forces of cavities and magnetic elements. The linear space charge fields are described analytically for the uniformly charged hard edge cylinders, and incorporates an off-axis expansion of the transverse electric field. The correlated emittance is then computed as $\tilde{\varepsilon}_{\mathrm{cor}} = 1/2[\langle r^2\rangle\langle r'\rangle^2 - \langle rr'\rangle]^{1/2}$, where $r' = dr/dz$ and the average is performed over the ensemble of slices.
The macroparticle code ASTRA [2], which incorporates a space charge algorithm on a rotational symmetric mesh, has been used for subsequent optimization of the injector. ASTRA allows the simulation of arbitrary cylindrical symmetric particle distributions and includes non linear fields. For typical optimization runs 1000 macroparticles have been used and once an optimum was obtained, runs with up to 4000 macroparticles, a number chosen after a convergence study of the beam parameters at the injector exit, have been performed. HOM-

[1] Throughout this report normalized transverse emittances will be quoted.

DYN and ASTRA show a general agreement. The small disagreements are understood as contributions of non linear space charge forces, especially in the cathode region, that are not taken into account in HOMDYN. A comparison of ASTRA and HOMDYN results is included in the Appendix.
When space charge forces are not anymore a concern, i.e. after acceleration in the first accelerator module, the 6D-tracking code ELEGANT [3] is used to optimize the optical functions of the lattice and track phase space distributions generated with ASTRA further downstream.
The bunch compression is investigated using the program TraFiC^4 [4] which includes the self-field of the beam and radiative self-interactions (i.e. via coherent synchrotron radiation). The retardation effects are simulated in a self-consistent approach.

2.2 Basic Layout of the Gun Section

The gun section is composed of a 1+1/2 cell photoemission based RF gun [8] (f =1.3 GHz) and a solenoid lens followed by a drift of proper length to allow the so-called "emittance compensation" process to take place [15]. A bucking coil behind the gun compensates the solenoid field at the cathode position. The gun with the solenoids is sketched in Fig. 1. The RF gun consists of a cylindrically symmetric cavity with an on-axis coaxial RF coupler. The on-axis coupler avoids RF field asymmetries (dipole and higher order) which can lead to a significant emittance growth. Similarly to the Tesla Test Facility (TTF) injector, Cs_2Te photocathodes [6] will be employed, illuminated by a laser with a wavelength of $\lambda = 262$ nm. Given the quantum efficiency of Cs_2Te photocathodes ($\sim$0.5%), 1 μJ of UV laser energy is sufficient to produce the required maximum charge of 1 nC. A sufficient overhead to produce even higher charges (up to 4 nC) will be provided. The laser will generate variable pulse structures (see Table 1). Since the maximum number of pulses per bunch train is 11500, the total laser energy should be 11.5 mJ per train. For a train repetition rate of 5 Hz, an average power of 55 mW is required. All these requirements have already been achieved at the TTF [5]. The laser should produce a radially and longitudinally uniform photon density on the photocathode. This type of distribution is preferred for the reduced impact on the beam emittance, since the transverse space charge forces within the bunch remains linear. An upgrade of the TTF laser will bring the rise time close to the required values. Even better rise times will be provided by a new laser system under construction for the photoinjector test stand [7].

2.3 RF gun Operating Point

The first task of the optimization procedure is to find a suitable set-up for the RF gun, e.g. the RF and the laser parameters. The free parameters are: the maximum electric field E_o in the cavity (at the position of the cathode), the launch phase of the laser ϕ_{RF} and the pulse duration σ_t and spot size σ_r of the laser. Henceforth a laser with a pure radially and

Wavelength	262 nm
Energy on photocathode/bunch	1 μJ
Train rep. rate	5 Hz
Pulse train length (max.)	1070 μm
Nb. of bunches per train (max.)	11500
Pulse spacing (min.)	93 ns

Table 1: Requirements on the photoinjector laser.

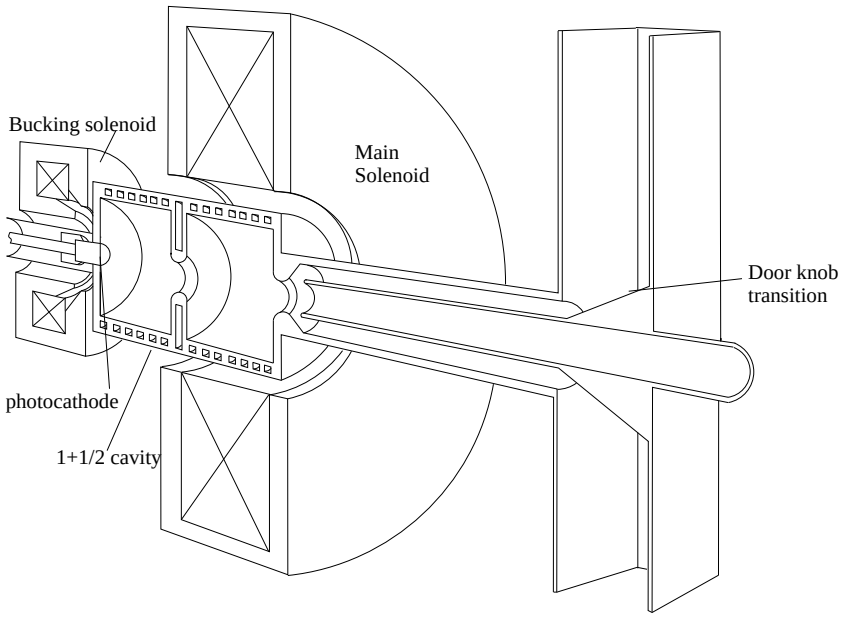

Figure 1: Cross sectional view of the RF gun along with the main and bucking solenoid and the RF input coupler.

longitudinally uniform distribution will be assumed, deviations from these assumptions are studied later in this report.
The maximum cavity field E_o should be as high as possible to provide the highest possible acceleration and thereby reduce the beam blow up induced by space charge. In the present case the emittance blow-up is due to space-charge: RF induced emittance growth is negligible (at least one order of magnitude lower). It is planned to run the L-band cavity with a peak gradient of 60 MV/m on the cathode (corresponding to an average gradient of 30 MV/m). Gradients of 80 MV/m have already been achieved, but not for the long RF pulses desired for FEL operation [11]. A standard TESLA 10 MW L-band klystron will be required to power the gun. The laser emission time w.r.t. the RF, i.e. the launch phase, is chosen close to the phase which provides the maximum energy gain and then further optimized in iterative simulations.
The pulse length of the laser primarily impacts the bunch length (and consequently the longitudinal emittance), but it also affects the transverse emittance due to the space charge forces scaling with the current within the bunch. In order to find the optimum settings for the

spot size of the laser beam on the cathode σ_r and the pulse length of the laser L_t 2D-scans of these parameters have to be performed and the beam parameters have to be analyzed downstream of the gun, for example at $z = 1\,\mathrm{m}$ from the photocathode. The complication of this procedure is, that the emittance at this location is largely due to correlations which can be removed further downstream. (See the discussion in the next section.) Result of these scans are presented in Fig. 2 for three different laser launch phases. The calculated

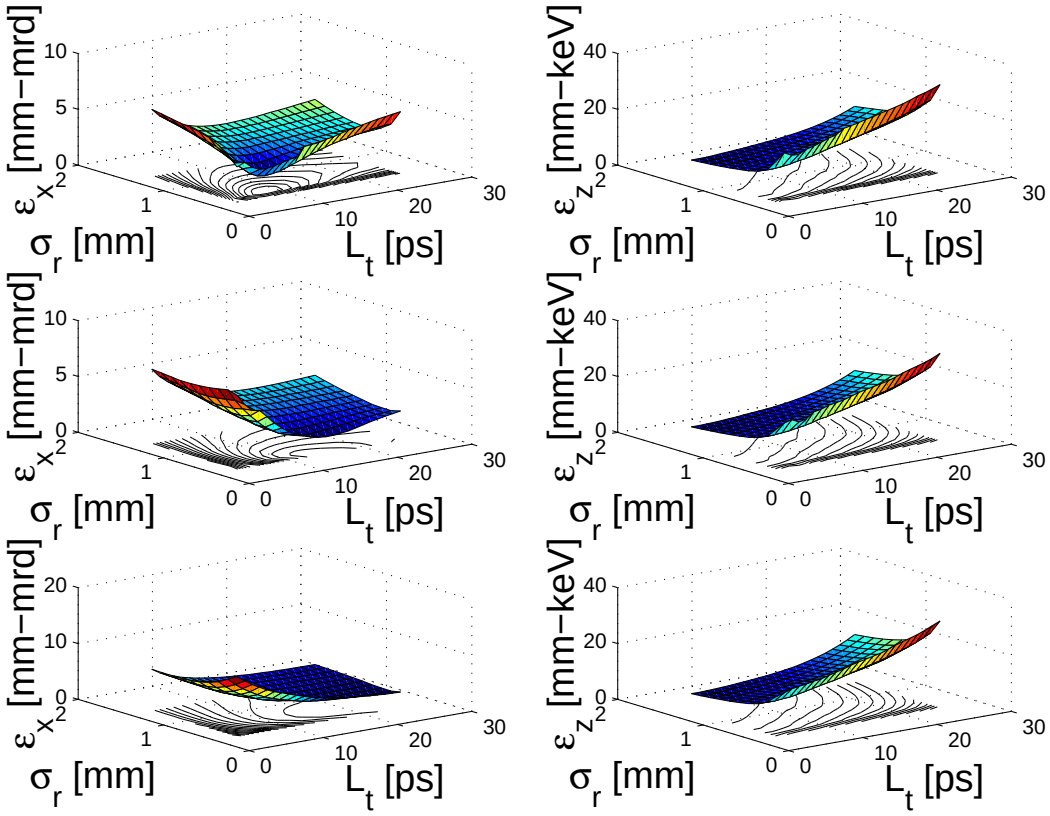

Figure 2: Two dimensional transverse (left column) and longitudinal (right column) emittance scans for three different laser launch phases: (from top to bottom row) 40, 44, and 48°. L_t denotes the total pulse length of the uniform pulse profile.

beam parameters result only from the interplay of space charge forces and RF focusing since no external magnetic field is applied for this study.[2] A short laser pulse and a large spot size of the laser beam lead to a low longitudinal emittance, independent of the launch phase. The projected transverse depends on the other hand emittance strongly on the launch phase and reaches a minimum for certain settings of the pulse length and radius. In order to understand the dependence of the uncorrelated part of the emittance on the initial parameter settings, it is possible to remove numerically the correlated emittance contributions to the transverse emittance, which dominate the parameter dependence at this position of the beam line. Fig. 3 shows the projected transverse emittance and the so-called reduced transverse

[2]For large σ_r and depending on the electric field in the cavity, the RF induced emittance growth can become significant. For the operating conditions considered in this report, the emittance growth is dominated by space charge effects.

emittance, which is calculated after removal of linear and quadratic correlations of r, p_r and z. Note the different scales on the emittance in both columns. The reduced transverse

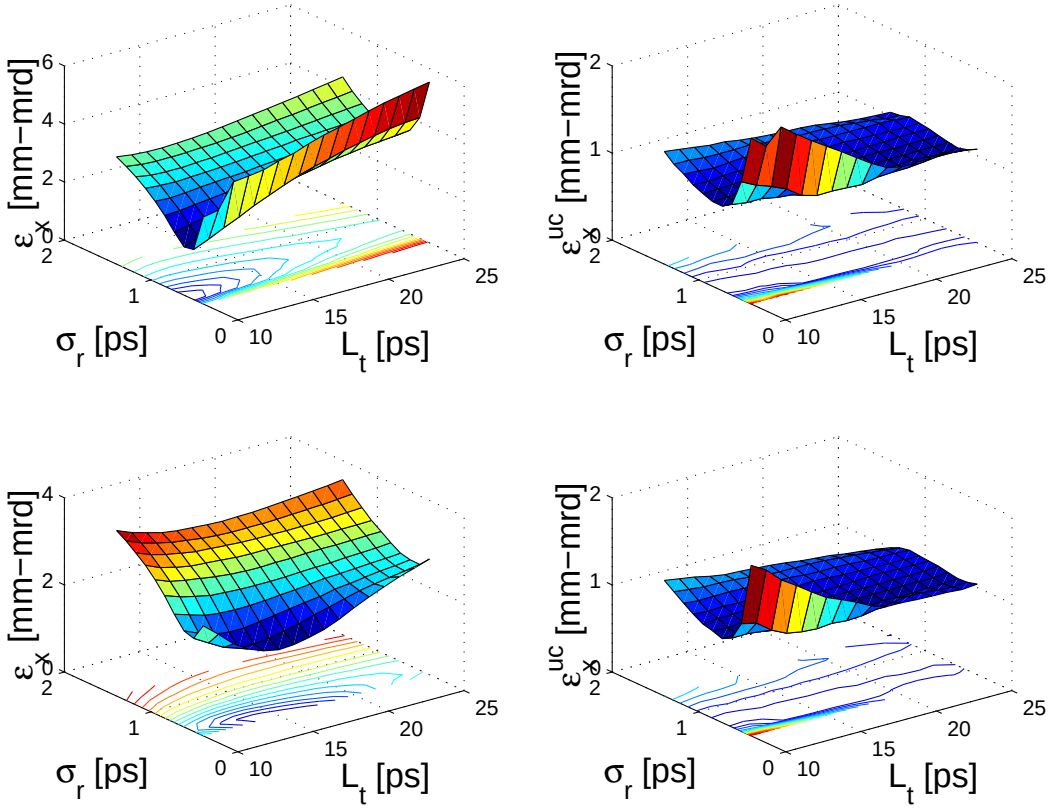

Figure 3: Two dimensional transverse emittance scans for two different laser launch phases: 40° (top row) and 44° (bottom row). The left column displays the projected transverse emittance, the right column displays the emittance calculated after removal of linear and quadratic correlations of r, p_r and z. L_t denotes the total pulse length of the uniform pulse profile.

emittance is independent of the launch phase, decreases with increased pulse length and is at least for longer pulses nearly independent of the spot size. The independence on the spot size for longer bunches is expected, since the transverse space charge force of a long bunch scales with $1/\sigma_r$ while the emittance is proportional to σ_r. Thus both effects cancel at least in the linear approximation.
For the choice of the laser spot size also the thermal emittance, i.e. the emittance which is generated in the cathode due to the emission process, has to be considered. Theoretical estimates indicated an upper limit of the thermal emittance of [9]:

$$\varepsilon_{th} = \frac{\sigma_r}{\sqrt{3}}\sqrt{2K/m_e c^2}, \tag{1}$$

where K is the average kinetic energy of the emitted electrons. While the thermal emittance calls for a small spot size, the reduced emittance has a shallow optimum at about 0.75 mm, which gives also reasonable values for the projected emittance. Table 2 collects

initial parameter settings as obtained after further optimization of the complete beam line. Here a perfectly rectangular longitudinal laser pulse has been assumed. The discussion of the impact of a small rise time at the head and the tail of the pulse follows at the end of this section for the case of optimal parameter settings of all beam line elements.

Parameter	Value	unit	comment
laser rms spot σ_r	0.75	mm	radially uniform distribution
thermal emittance contribution	0.74	mrad mm	estimated upper limit
total laser pulse length L_t	20	ps	uniform distribution
E_o	60	MV/m	
ϕ_{RF}	44	°	

Table 2: Parameters of the RF photocathode gun.

2.4 Optimization of the Emittance Compensation Process

A solenoid is located close to the cathode in order to control the beam envelope, which tends to be divergent due to the presence of space charge forces. Though it provides focusing, it also contributes to a reduction of the correlated emittance via the so-called emittance compensation process [15]. This technique for the compensation of correlated emittance contributions has been experimentally demonstrated at the Accelerator Test Facility (ATF) at BNL [17]. The underlying argument for such a compensation mechanism is as follows (see Fig. 4): In an RF gun, operating in the space charge dominated regime, most of the emittance growth is due to the space charge forces, which introduce correlations between the phase space r, p_r and the longitudinal position z (i.e. the space charge field variation along z results in different transverse betatron phase advances for different longitudinal slices of the bunch). Typically the space charge field is stronger in the longitudinally central slices than towards the ends of the bunch. Correspondingly the center slices will have a higher radial momentum p_r. With a properly tuned solenoid it is possible to introduce a focusing kick which will, after a drift of proper length in which the space charge force acts again, result in a cancelation of the correlation induced by space charge. After reaching a minimum the emittance would grow again under the influence of the space charge in a drift section. To circumvent this the final phase of the compensation process has to take place in an accelerating section, so that the minimum emittance is reached at higher energy where the space charge force is sufficiently suppressed. The peak magnetic field of the solenoid, the length of the downstream drift and the gradient of the accelerating cavity (booster) are chosen to provide a proper matching condition for the beam. One possible matching technique is based on the so-called "invariant envelope" [16]: The beam should be at a laminar waist at the booster linac entrance (i.e. $\sigma_r' = 0$) and the energy gain in the booster γ'_{boost} should be related to the rms beam size σ_w, the incoming mean beam energy γ and the

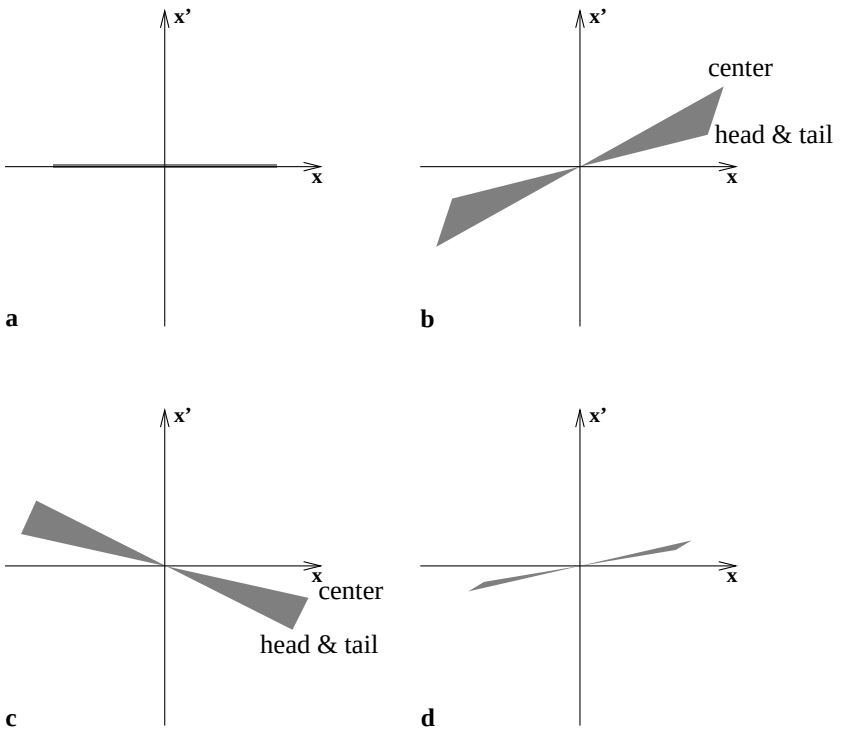

Figure 4: Transverse phase space plots showing schematically transverse emittance growth and reduction due to space charge forces. (a) Initial phase space with small (zero) emittance at the gun. (b) Phase space after transport up to the solenoid lens, showing the growth of the projected emittance due to the different focusing strength at the bunch center and the tails. (c) The phase space distribution has been rotated by an external focusing kick. (d) Phase space after a drift behind the lens. The projected emittance is decreased due to the action of the space charge forces.

peak current $\hat{I}$ via the relation:

$$\gamma'_{boost} = \frac{2}{\sigma_w}\sqrt{\frac{\hat{I}}{3I_o\gamma}}, \tag{2}$$

where I_o is the Alvfèn current (17 kA for electrons). This equation insures that the beam envelope is matched to the "invariant envelope", an envelope solution which has the property to reduce simultaneously the beam spot size and the transverse momentum. Thus when injected onto this envelope, the transverse emittance is expected to decrease. A more specific operation point, which is also applied here, has been found recently [21] in the context of the LCLS FEL [22]. In the drift behind the gun and the solenoid the emittance decreases for most parameter settings not to a single minimum, but shows two minima separated by a local maximum. For a certain setting of the solenoid the local maximum of the emittance is located at the position of a waist of the beam envelope, as displayed in Fig. 5. If this setting is found, the entrance of the accelerating cavity is placed at the location of the the minimum of the beam envelope and the accelerating gradient is chosen according to Eq. (2).
Different schemes for the beam acceleration have been considered. For example a single

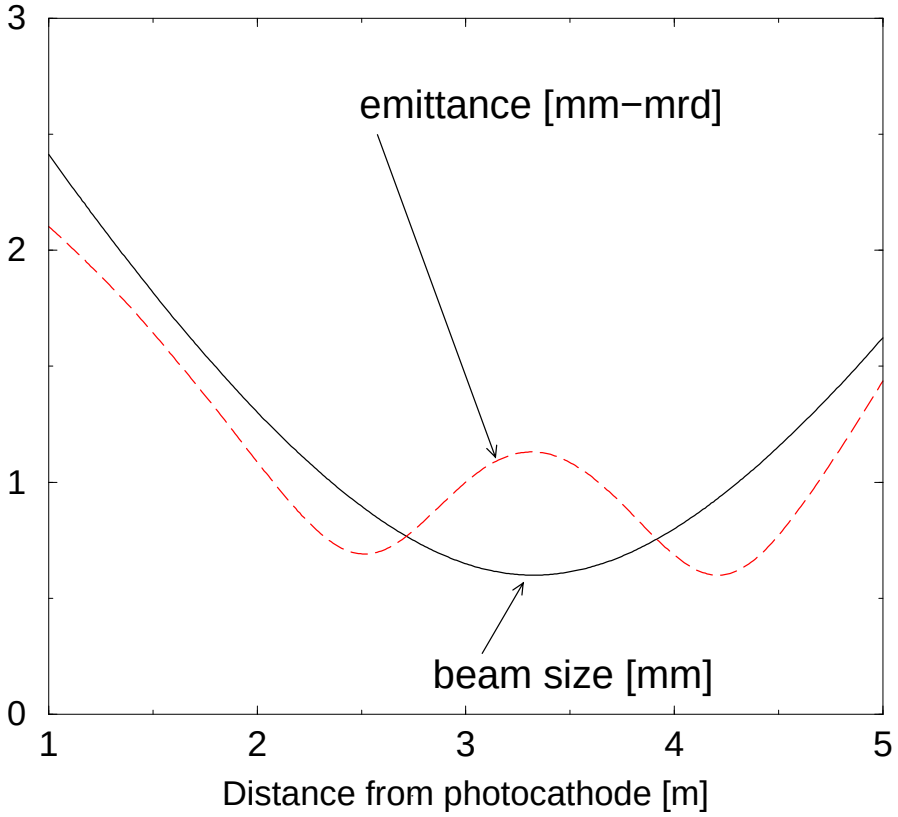

Figure 5: Development of the transverse beam emittance and the beam envelope in a drift space for the working point of the RF gun. The accelerating cavity will be placed at the location of the beam waist, i.e. at the emittance maximum.

booster cavity as it is in use at the TTF. A low emittance was indeed obtained downstream of the booster, but due to the low energy it increased again further downstream. Instead it is now foreseen to inject the beam directly into a complete TESLA module of eight superconducting 9-cell cavities [19].
Solenoids designed for the injector test facility PITZ [20] have been used for the simulations. The solenoid system consists of a main solenoid that can be located around or downstream of the gun cavity, and a bucking coil located just upstream of the photocathode back plate in order to zero the field on the photocathode surface. A non-zero magnetic field on the photocathode surface would result in a significant emittance contribution of

$$\varepsilon_{\mathrm{MAGNETIC}} = \frac{e}{2m_e c} \cdot B_z^{\mathrm{photocathode}} \sigma_r^2. \tag{3}$$

The equation is valid for a radially uniform beam distribution. Several configurations of solenoids, e.g. different distances of the main solenoid from the photocathode have been investigated. The on-axis magnetic fields $B_z(z, r = 0)$ computed with the POISSON [18] code are presented in Fig. 6 for different configurations of the main and bucking solenoids. The longitudinal solenoid position, its strength, the length of the drift and the gradient of the booster cavity were found to be closely related, if the above described matching criterion is applied. The further downstream the solenoid is positioned, the longer the drift to the

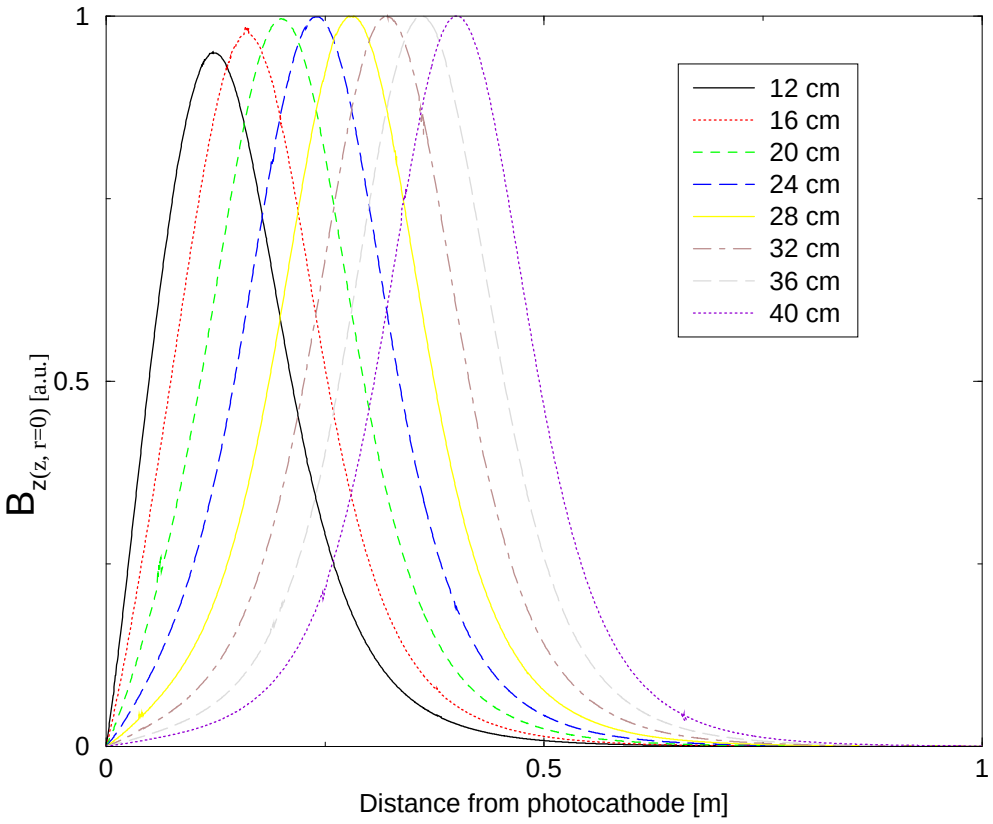

Figure 6: On-axis longitudinal magnetic field for different configurations of the main and bucking solenoids.

booster has to be. The spot size at the waist is getting larger and therefore the required gradient of the booster is getting lower for an increased distance of the solenoid to the cathode. The final emittance is basically independent of the solenoid position, but the sensitivity of the emittance to the field strength of the solenoid is somewhat lower if the solenoid is located closer to the cathode. Fig. 7 shows the waist location z_w and the beam size at the waist σ_w versus the solenoid strength for two positions of the maximum magnetic field (20 cm and 40 cm w.r.t. the cathode). While the beam size at the waist decreases with increasing focusing fields, the position of the waist shifts downstream for increased focusing strength in case of low focusing fields. This is due to the increased space charge force which counteracts the external focusing. After reaching a maximum distance the position of the waist shifts upstream again for increased focusing fields as in a case without space charge. The above defined operating point, where the beam waist is at the position of the local emittance maximum is in both cases on the falling branch of the waist position, not far from its maximum. The benefit of the downstream location of the solenoid is the increased drift length, which is desired to incorporate diagnostic components and the cold-warm transition of the superconducting accelerator module, and the reduced gradient which facilitates a stable operation of the injector. Based on these considerations the solenoid center will be located at z =0.40 m from the photocathode. The laminar waist is then achieved at $z \simeq$3.5 m. Starting with a gradient of 12 MV/m, in accordance to Eq. (2), the gradient was further optimized in simu-

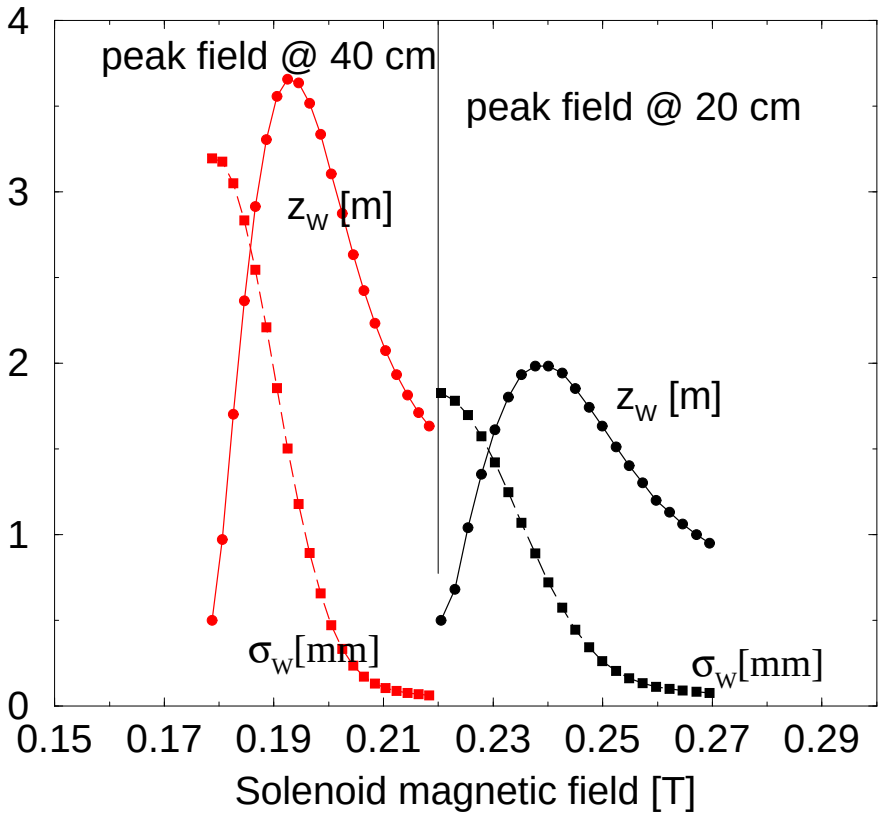

Figure 7: Variation of σ_w and z_w versus the peak magnetic field for two locations of the solenoid center (20 and 40 cm from the photocathode).

lations to 11.5 MV/m for the first four cavities and the highest possible gradient of 25 MV/m for the next four cavities. Transverse emittances of 0.5 mrad mm[3] were obtained (see Fig. 10) at a kinetic beam energy of $\simeq$140 MeV, an energy high enough to insure that the beam is emittance dominated.

2.5 Correction of Longitudinal Phase Space Distortions

A general problem of RF guns is the coupling of the transverse and the longitudinal emittance. In order to reduce the transverse emittance the bunch length generated in the gun should be long, but this leads to an increased longitudinal emittance. While the increase in the gun might still be tolerable, the emittance growth introduced by the cosine-like RF potential in the subsequent acceleration section is generally intolerable, since the RF induced longitudinal emittance scales like the bunch length to the power of three. A possibility to decouple the transverse from the longitudinal emittance in the gun is an additional magnetic bunch compression section at the lowest possible energy, as it is set up at the TTF. The required interruption of the accelerating structure, the transverse focusing of the dipoles in

[3]The quoted number is the projected emittance and does not account for the thermal emittance.

the bunch compressor, which needs to be controlled by wedge angles (which may in turn disturb the chromatic properties of the compressor section) and, finally, the reduced bunch length behind the compressor lead to increased space charge effects which are difficult to control. Therefore a scheme where the non linearities introduced by the RF are compensated at high energy in front of the first bunch compressor by means of a 3^{rd} harmonic accelerating section is foreseen for the XFEL injector [14]. An additional advantage of the 3^{rd} harmonic section is, that it can also be used to compensate for non linearities of the subsequent bunch compressor section. Fig. 8 shows the highly distorted longitudinal phase space at the exit of the accelerator module. The operating point for the correction of the the non linearity of

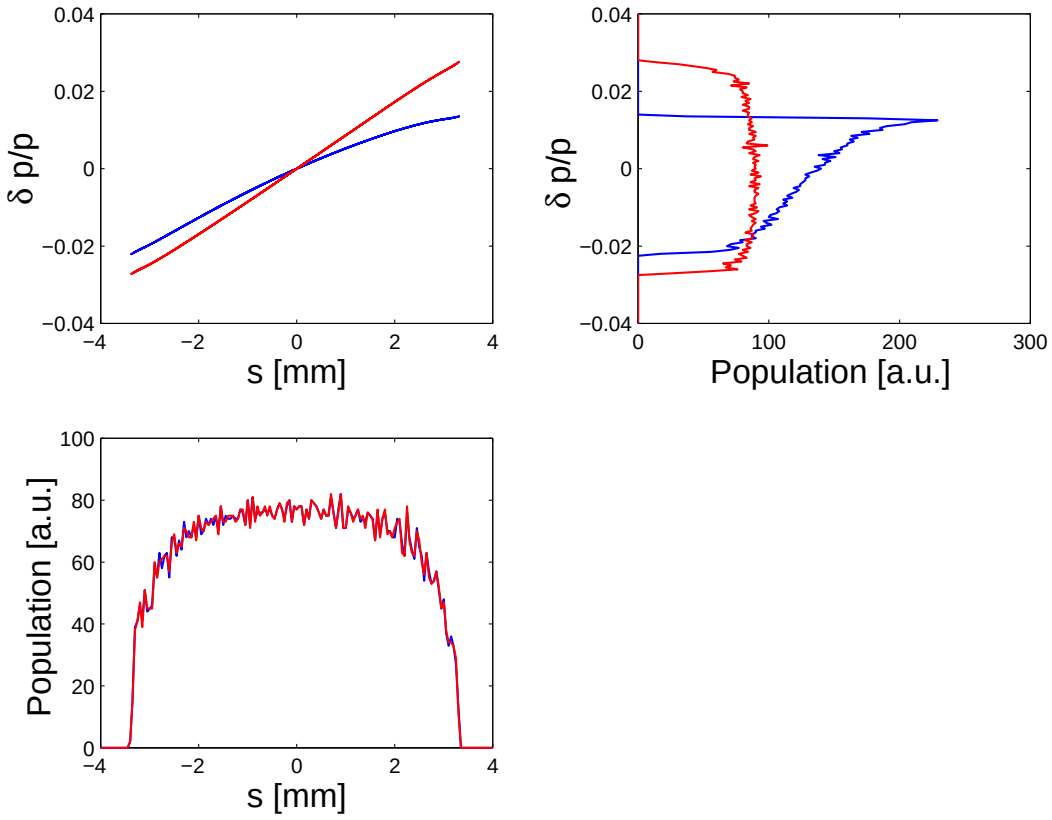

Figure 8: Longitudinal phase space at the exit of the accelerator module (blue) and downstream of the third harmonic RF section (red). The longitudinal phase space distribution is linearized by the combined action of the first and third harmonic RF. The remaining curvature is matched to the second order compression factor of the bunch compressor.

the longitudinal phase space, (i.e. the amplitude V_3 and the phase φ_3 of the 3^{rd} harmonic section,) is closely related to the booster linac parameters (V_1, φ_1): Given the incoming kinetic energy E_0 (at the gun exit), the relative energy spread at the exit of the 3^{rd} harmonic section takes the form:

$$\begin{aligned}\delta(s) \;=\; & \frac{1}{E_0 + V_1\cos(\varphi_1) + V_3\cos(\varphi_3)} \cdot \left[V_1\left(\cos(k_{rf}s+\varphi_1)\right.\right. \\ & \left.\left. -\cos(\varphi_1)\right) + V_3\left(\cos(3k_{rf}s+\varphi_3) - \cos(\varphi_3)\right)\right], \end{aligned} \tag{4}$$

where s is the longitudinal coordinate w.r.t. the bunch center.
On the other hand, a downstream compression section (i.e. a single bunch compressor or a chain of bunch compressors) maps an electron with initial position (s_i, δ_i) to (s_f, δ_f) according to:

$$s_f = s_i + R_{56}\delta_i + T_{566}\delta_i^2 + U_{5666}\delta_i^3 + \mathcal{O}(\delta_i^4) \text{ and } \delta_f = \delta_i, \tag{5}$$

where the Taylor coefficients of the transfer map are written as: $R_{56} = \partial S^{i\to f}/\partial\delta$, $T_{566} = 1/2\partial^2 S^{i\to f}/\partial\delta^2$, and $U_{5666} = 1/6\partial^3 S^{i\to f}/\partial\delta^3$, defining $S^{i\to f}$ as the path length through the compressor. Note that the maximum compression occurs when $s_f = 0$ in equation 5.
The longitudinal phase space upstream of the compressor can be expanded in the polynomial form $\delta(s_i)$:

$$\delta(s_i) = \alpha_1 s_i + \alpha_2 s_i^2 + \alpha_3 s_i^3 + \mathcal{O}(s_i^4) \tag{6}$$

From Eq. (6) and Eqns (5) the three longitudinal matching conditions

$$\alpha_1 = \frac{-1}{R_{56}},\ \alpha_2 = -\alpha_1^2\frac{T_{566}}{R_{56}} \text{ and } \alpha_3 = \frac{1}{R_{56}}\left(-\alpha_1^3 U_{5666} + 2\alpha_1\frac{T_{566}^2}{R_{56}}\right) \tag{7}$$

can be derived. The coefficients α_i are the successive derivatives of $\delta(s)$ in s at the origin,

$$\alpha_i \overset{def}{=} \frac{1}{i!}\left[\frac{\partial^i\delta(s)}{\partial s^i}\right]_{s=0} \tag{8}$$

which applied to Eq. (4) and using the matching conditions which constitute Eq. (7) yield the system of equations:

$$\begin{aligned} V_1\sin(\varphi_1) + 3V_3\sin(\varphi_3) &= \hat{A}\left(E_0 + V_1\cos(\varphi_1) + V_3\cos(\varphi_3)\right) \\ V_1\cos(\varphi_1) + 9V_3\cos(\varphi_3) &= \hat{B}\left(E_0 + V_1\cos(\varphi_1) + V_3\cos(\varphi_3)\right) \\ V_1\sin(\varphi_1) + 27V_3\sin(\varphi_3) &= \hat{C}\left(E_0 + V_1\cos(\varphi_1) + V_3\cos(\varphi_3)\right), \end{aligned} \tag{9}$$

where the unknowns are φ_3, φ_1 and V_3, since V_1 is determined from other considerations, e.g. one may desire the highest possible energy gain, or in the case of a RF photoinjector booster, V_1 should be chosen in accordance to the invariant envelope concept. The coefficients $\hat{A}, \hat{B}$ and $\hat{C}$ in Eq. (9) are defined as:

$$\hat{A} = \frac{-1}{k_{rf}}\alpha_1 \overset{\text{max. compr.}}{=} \frac{1}{k_{rf}R_{56}},\ \hat{B} = \frac{-\alpha_1^2 T_{566}}{2k_{rf}^2 R_{56}}, \text{ and}$$
$$\hat{C} = \frac{-\alpha_1^3}{6k_{rf}^3 R_{56}}\left(U_{5666} - 2\frac{T_{566}^2}{R_{56}}\right) \tag{10}$$

From the latter equations, the accelerating voltage and phase of the 3^{rd} harmonic section can be derived as a function of the parameters of the fundamental accelerating section:

$$V_3 = \sqrt{\left(\frac{V_1\sin(\varphi_1)\left[1 - \hat{A}/\hat{C}\right]}{3\left[9\hat{A}/\hat{C} - 1\right]}\right)^2 + \left(\frac{BE_0 - (1-\hat{B})V_1\cos(\varphi_1)}{9 - \hat{B}}\right)^2}, \tag{11}$$

$$\tan(\varphi_3) = -\frac{V_1\sin(\varphi_1)(1 - \hat{A}/\hat{C})(9 - \hat{B})}{3(\hat{B}E_0 - (1-\hat{B})V_1\cos(\varphi_1)(1 - 9\hat{A}/\hat{C})}. \tag{12}$$

The phase φ_1 is obtained, after elimination of V_3 and φ_3, by solving a second order equation of the form $\mu\xi_1 + \nu\sqrt{1-\xi_1^2} = \kappa$ with $\xi_1 = \sin(\varphi_1)$; the solution takes the form:

$$\xi_1^{\pm} = \frac{\mu\kappa \pm \nu\sqrt{\mu^2+\nu^2-\kappa^2}}{\mu^2+\nu^2}, \tag{13}$$

where the coefficients are $\mu = (8\hat{A}V_1)/(9\hat{A}-\hat{C})$, $\nu = (8\hat{A}V_1)/(\hat{B}-9)$, and $\kappa = 9\hat{A}E_0/(9-\hat{B})$. The solution ξ_1^+ is not physical, since $\xi_1^+ > 1$. From the ξ_1^- solution on gets:

$$\varphi_1 = \arcsin\left(\frac{\mu\kappa - \nu\sqrt{\mu^2+\nu^2-\kappa^2}}{\mu^2+\nu^2}\right). \tag{14}$$

The Eqns 11 and 14 are used henceforth to find the optimum set-up of the first and 3^{rd} harmonic section given an amplitude for the accelerating field V_1 and an incoming beam energy E_0.

In the TESLA XFEL accelerator the compression scheme is performed in three stages. Considerations of Coherent Synchrotron Radiation (CSR) effects [13] and the staged compression scheme require an incomplete compression in the first bunch compressor. Thus, the analysis aforementioned is not exactly applicable, since it assumes a full compression in the first bunch compressor. Moreover the non linearities introduced by space charge forces and the RF field of the gun are not taken into account. The set-up of the accelerating section and the 3^{rd} harmonic section was calculated using the aforementioned relations and then further optimized by means of numerical simulations using ASTRA and ELEGANT. The figure-of-merit was a linear longitudinal phase space behind the bunch compressor. Fig. 8 shows the phase space before and behind the 3^{rd} harmonic section. The remaining curvature in phase space behind the 3^{rd} harmonic section is matched to the T_{566} of the bunch compressor.

2.6 Control of the Transverse Beam Envelope in the Acceleration Section and the Third Harmonic Section

The main focusing element in the beam line described up to now is the main solenoid in the gun section. Some focusing is provided by the RF accelerating section and some defocusing by the 3^{rd} harmonic RF section. The set-up leads to rather large beta functions ($\simeq 80\,\mathrm{m}$) at the matching triplet into the bunch compressor ($z = 19\,\mathrm{m}$). For the bunch compression a large correlated energy spread of 1.5% is introduced by operating the accelerating section off-crest. In order to avoid a significant chromatic emittance dilution in the triplet, the beta function is decreased by means of another solenoid lens located between the 8^{th} cavity and the 3^{rd} harmonic section. The beta function in the triplet is reduced to $\simeq$40 m, which avoids a significant chromatic emittance dilution in the triplet (see Section 2.9). The beta function at the solenoid position is ($\simeq 80\,\mathrm{m}$) but a weak focusing is required only.

2.7 Nominal Set-up and Achieved Parameters

The parameter settings of all beam line components was optimized in iterative simulation runs. The final beam line settings and element locations are collected in Table 3. The corresponding phase space and beam parameters at z =18 m from the photocathode are displayed in Fig. 9 and Table 4, respectively. The evolution of the beam envelope and longitudinal beam parameters along the beam line are shown in Figs 10 and 11.

Element	Location [m]	Setting	unit
Gun	0.00 (cathode location)	$\hat{E}_z$=60 ϕ_o=44	MV/m °
Solenoid	0.40 (peak field location)	$\hat{B}_z$=0.198	T
Accelerating Section	3.95 (center of the first cavity)	$E_{z,1}$=11.50 (first 4 cav.) $E_{z,1}$=25.00 (last 4 cav.) φ_1=-16.03	MV/m MV/m °
3^{rd} Harm. Section	15.00 (center of the first cavity)	$E_{z,3}$=13.9 φ_3=-179.26	MV/m °

Table 3: Optimized beam line settings and element locations for the RF gun section, the acceleration section and the 3^{rd} harmonic section of the injector.

bunch length	σ_s	1.77	mm
average kinetic energy	E	142.4	MeV
rms energy spread	σ_E	2132.3	keV
transverse emittance	ε	0.43	mrad mm
transverse emittance incl. thermal emittance	$[\varepsilon^2 + \varepsilon_{th}^2]^{1/2}$	$\simeq$ 0.90	mrad mm
longitudinal beam emittance	ε_z	57.79	keV mm
beta function	$\beta_{x,y}$	43.5	m
alpha function	$\alpha_{x,y}$	5.2	–

Table 4: Beam parameters downstream of the third harmonic section ($z = 18$ m) for nominal parameter settings.

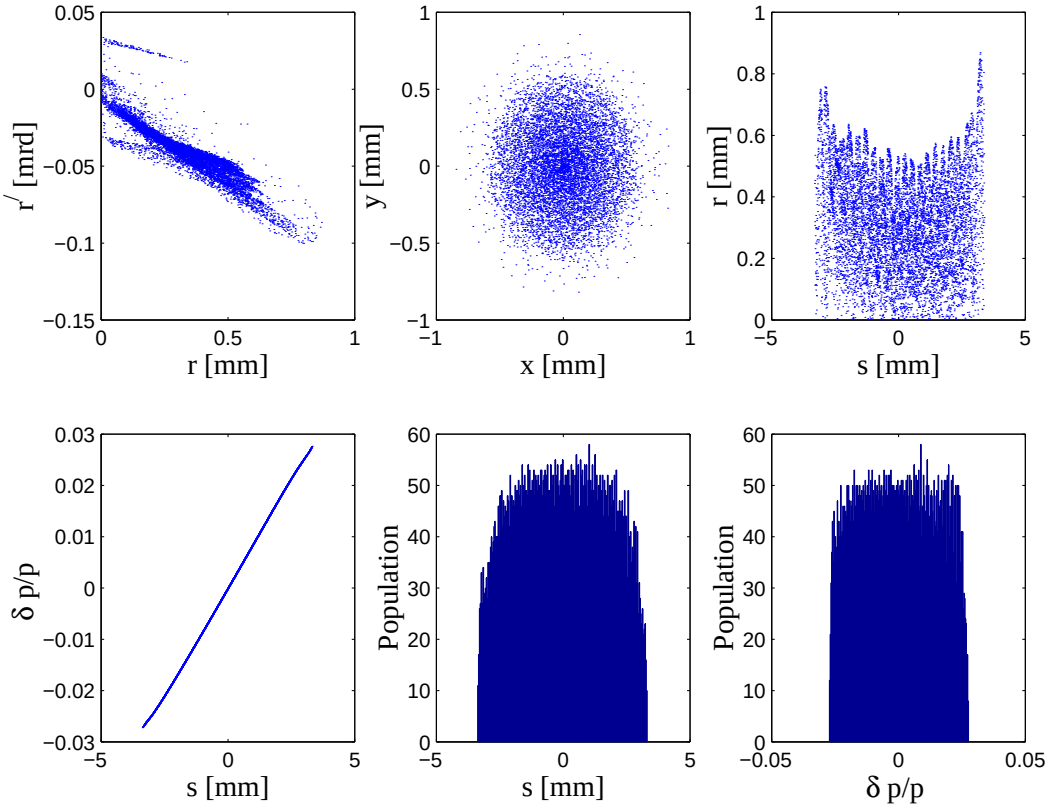

Figure 9: Phase space distributions at the injector exit (z=18 m).

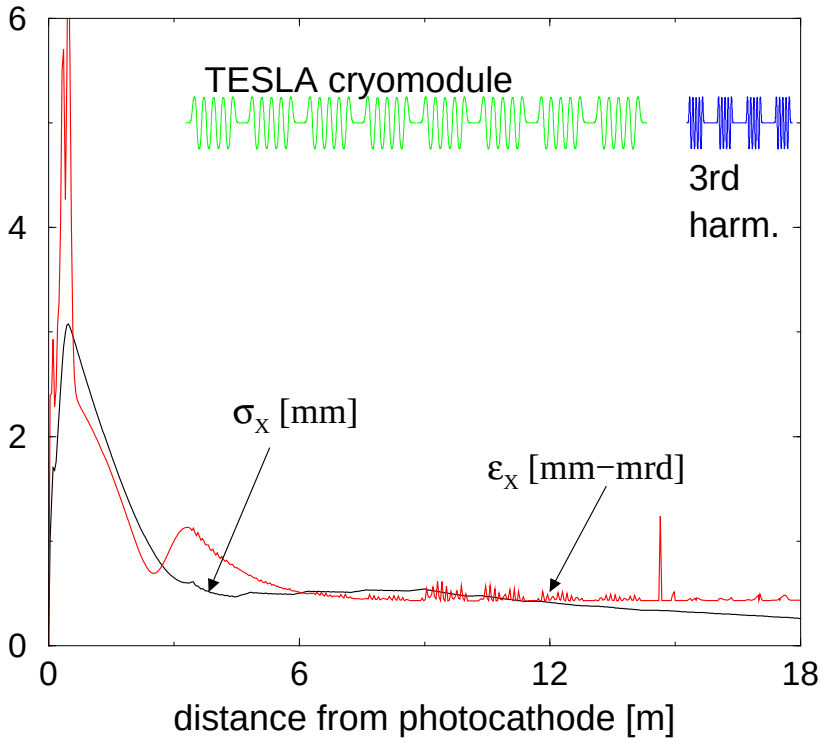

Figure 10: Transverse beam parameter evolution along the beam line from the photocathode up to the exit of the third harmonic section. The solenoid at z=14.5 m is optimized to lower the beta function at z =18 m.

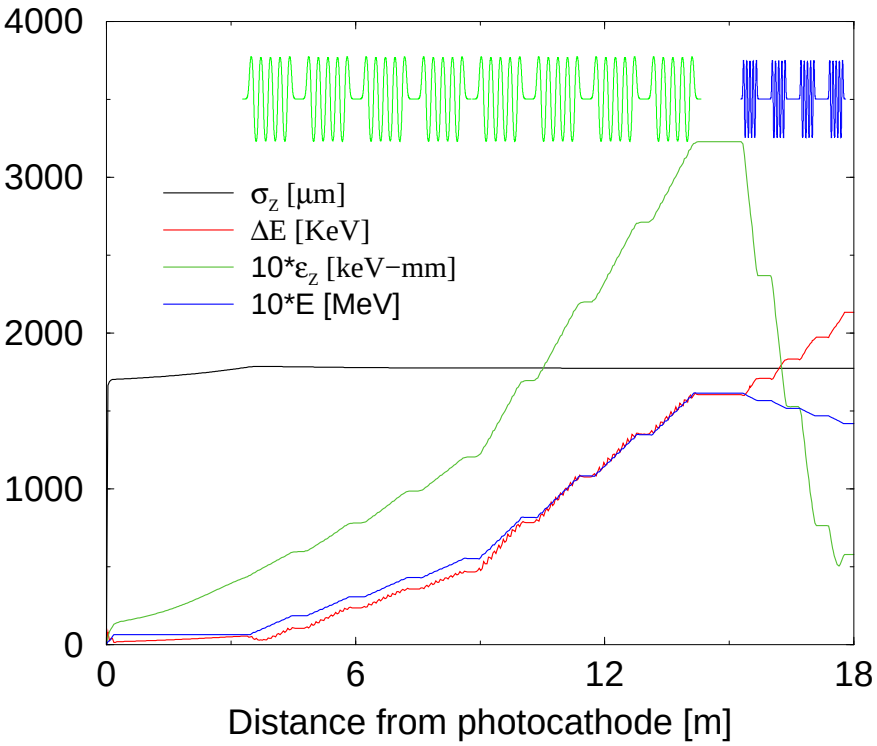

Figure 11: Longitudinal beam parameter evolution along the beam line from the photocathode up to the exit of the third harmonic section.

2.8 Impact of the Rise Time of the Laser Pulse

So far a perfect longitudinal laser pulse with zero rise time at the head and the tail of the pulse has been assumed. Fig. 12 and 13 show the effect of a small rise time on the transverse and longitudinal beam emittance. The effect of the rise time on the transverse emittance will in practice be covered by the thermal emittance, so that a rise time of $\leq$2 ps is tolerable. An upgrade of the TTF laser will bring the rise time close to the required values. Even better rise times will be provided by a new laser system under construction for the photoinjector test stand [7]. It should be noted, that the rise time effects the emittance of the head and tail slices of the electron bunch, while the central slices which are important for the FEL operation remain unaffected.

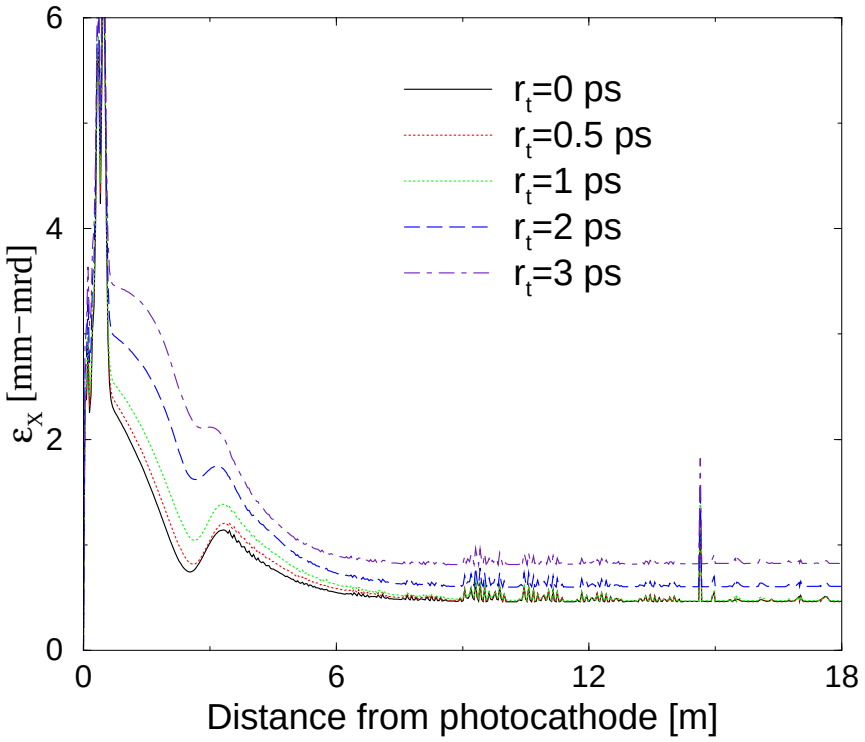

Figure 12: Sensitivity of the transverse emittance to the rise time of the laser r_t.

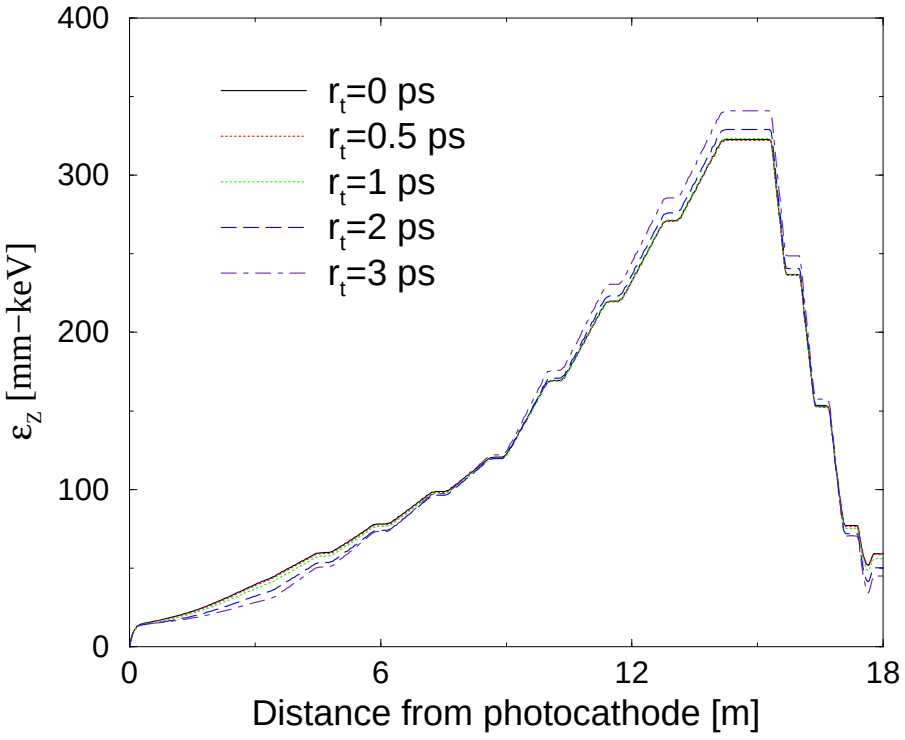

Figure 13: Sensitivity of the longitudinal emittance to the rise time of the laser r_t.

2.9 Matching and Bunch Compression Sections

2.9.1 General Considerations

Following the third harmonic RF section, the beam is compressed using an achromatic four-dipole chicane with variable momentum compaction. Under nominal operation the bending angle is 14.2 ° resulting in a momentum compaction of $R_{56} \simeq$-0.10 m. Downstream of the compressor a matching section follows: it allows the transverse matching of the beam into the subsequent accelerating section and also incorporates a diagnostics section. The total length of this section is approximately 20 meters; thus care has to be taken to avoid significant emittance blow-up which may be caused by (1) chromaticity, (2) CSR effects in the compressor area and (3) space charge forces especially in the F0D0 channel.
As far as chromaticity induced emittance growth is concerned, a general criterion is to have a low beta lattice with small absoulte quadrupole strength; a more formal rule is to make sure that the condition [24]:

$$\delta \cdot \beta_{x,y}|k|L_{\mathrm{QUAD}} \ll 1 \tag{15}$$

is satisfied. In the latter equation $\beta_{x,y}$ are the horizontal and vertical beta functions at the quadrupole of strength k and length L_{QUAD} and δ is the energy spread. Note that in this section the beam has a large energy spread of 1.5%, which is required for the bunch compression.
The emittance growth due to CSR effects and space charge forces will be discussed in the next sections.

2.9.2 Pre-compressor matching section and compression

The optics in the bunch compressor region has to be optimized to prevent emittance growth from coherent synchrotron radiation (CSR) effects [25]. The radiated CSR power depends on the bunch length and scales like $1/\sigma_s^{4/3}$. Therefore, especially for short bunches, CSR fields radiated on curved trajectories induce energy offsets in a necessary dispersive section; thus causing emittance growth.
The sensitivity of the correlated transverse emittance to energy offsets is described by the function $\mathcal{H}$, defined as:

$$\mathcal{H} = \frac{1}{\beta(s)}\eta^2(s) + \beta(s)\eta'^2(s) + 2\alpha(s)\eta(s)\eta'(s) + \frac{\alpha^2(s)}{\beta(s)}\eta^2(s). \tag{16}$$

$\mathcal{H}$ depends only on the magnetic lattice and becomes important in the third and the fourth bend of the magnetic bunch compressor, since these are the locations where the bunch length is minimal (see Fig. 14). Eq. (16) can be simplified by assuming a waist close to the third and fourth bending dipole, so that $\alpha \simeq 0$. In the fourth dipole the dispersion η is already small, while η' is still large (see Fig. 19) so that the emittance contribution in the magnet can be minimized by a minimal beta function. In the third dipole η and η' are of similar

order, so that the contribution is minimized for $\beta \simeq 1$.
For the growth of the slice emittance, more complicated details of the non linearities of the CSR fields have to be considered. Numerical simulations performed with the code TraFiC^4 have proven, that a waist between the third and fourth dipole minimizes also the slice emittance growth. In Fig. 16 the transverse emittance in the bending plane versus the strength of the upstream matching triplet is shown. The minimum emittance is reached when the beam envelope has a waist between the third and fourth bending dipole. The vertical beam envelope will additionally be focused by the compressor dipoles.
Even in case of this ideal matching the beam exhibits some emittance growth, which can be further reduced by suppressing the CSR radiation by "shielding". Most of the self-interaction of the bunch results from fields radiated at the retarded time at wavelengths in the sub-mm and mm regime, which are guided in the vacuum chamber. The propagation of the CSR spectrum above a cutoff wavelength is suppressed. Thus, the CSR effects can be reduced by reducing the vacuum chamber size in the vertical plane. The vacuum chamber is modeled as two infinite, parallel and conducting plates separated by the distance h. The cutoff wavelength is $\lambda_c \simeq 2[h^3/\rho]^{1/2}$, ρ being the curvature of the trajectory [26]. From the operational point-of-view the minimal tolerable chamber height is estimated to be 8 mm. Fig. 15 compares the energy loss and the energy spread generation along the compressor beam line for the free space and the shielded case. In both cases the horizontal beta function is set up in the same way, i.e. with a horizontal waist between the third and fourth dipole. The effect of the shielding on the beam emittance is shown in Fig. 16. The longitudinal and transverse phase space before and after compression is shown in Fig. 17.

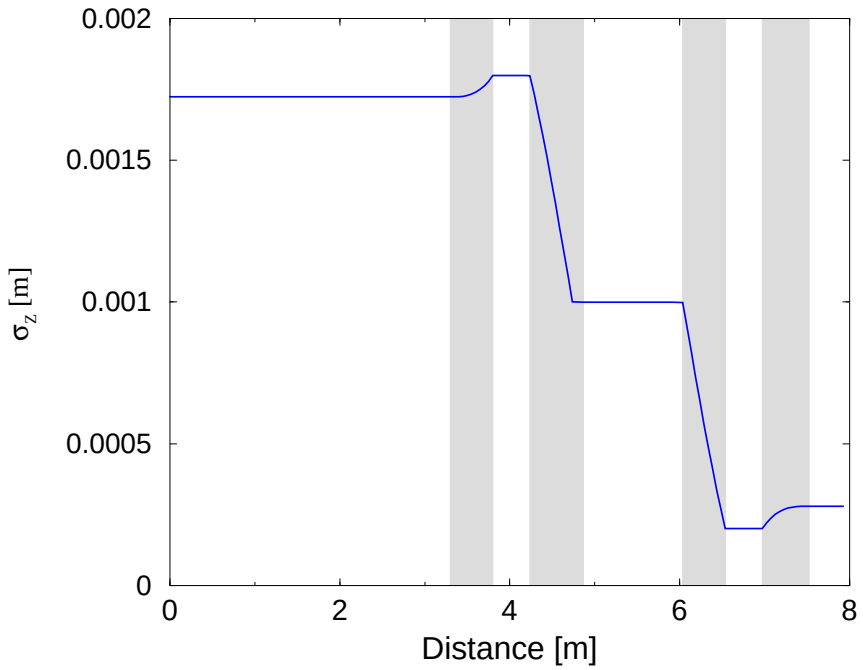

Figure 14: Bunch length evolution along the first bunch compressor. The shaded areas indicate the locations of the dipoles.

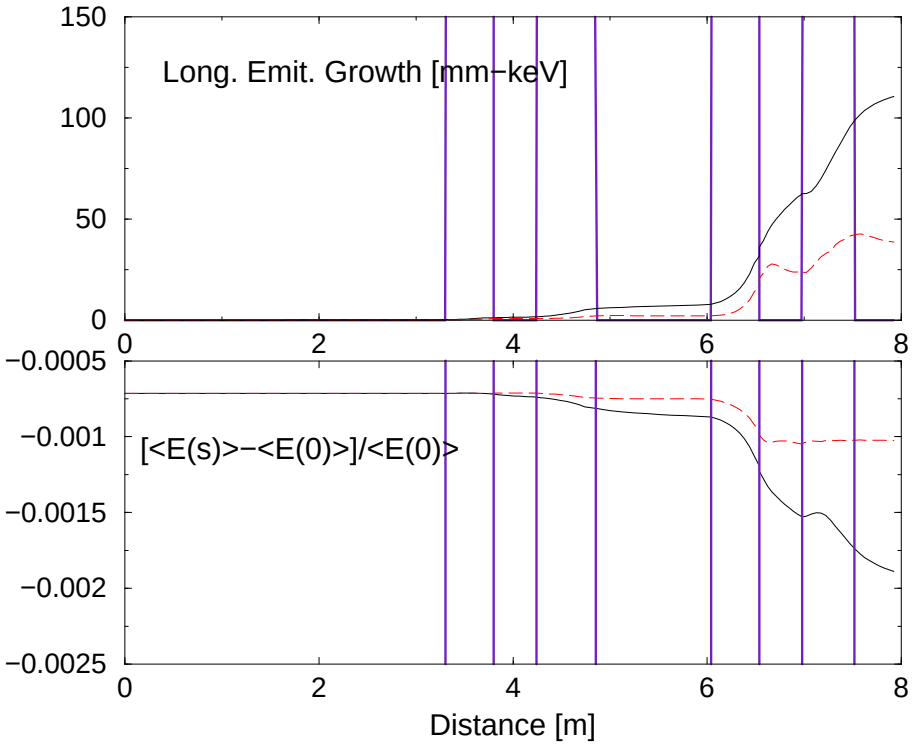

Figure 15: Energy spread generation (top) and energy loss (bottom) along the chicane for the shielded (dashed lines) and unshielded (solid lines) cases. The vertical lines indicate the locations of the dipoles.

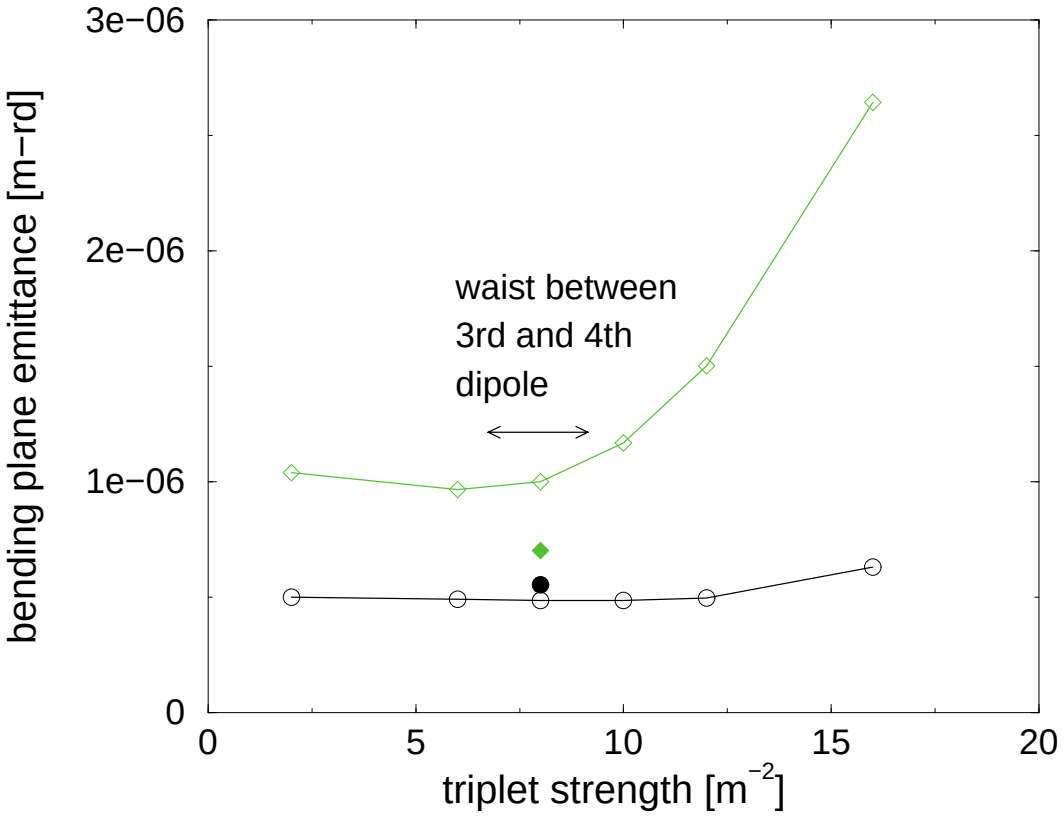

Figure 16: Emittance downstream of the first bunch compressor versus the upstream triplet strength. The circles and diamonds are the slice and the projected emittances, respectively. Open symbols are for the unshielded case, while filled symbols at k_1 =8 m $^{-2}$ are the emittances for the case of 8 mm shielding (see the text for details).

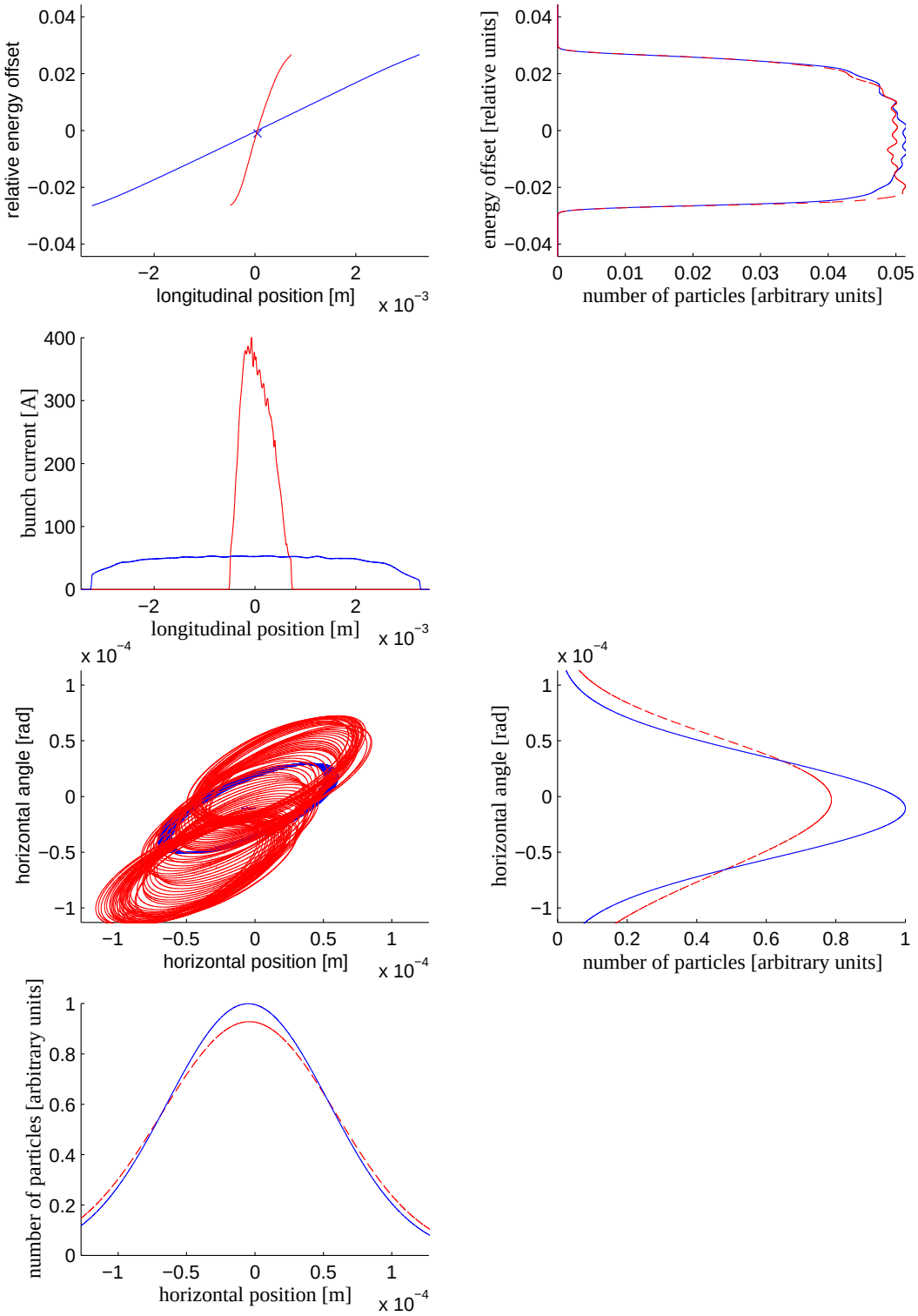

Figure 17: Longitudinal phase space before (blue) and after (red) Bunch Compressor 1 and transverse phase space at the compressor exit without (blue) and with (red) CSR, respectively. The shielding of a vacuum chamber with 8 mm height is taken into account.

2.9.3 Post-compressor matching section

The beam transport downstream of the compressor has two main functions. First the matching of the beam into the downstream accelerating sections (3 standard TESLA acceleration modules). Secondly it incorporates a diagnostics section which especially integrates an online emittance measurement (see Section 4.2.3). Besides the two aforementioned functions, the beam line also offers a wide tunability for diagnostics purposes. The beam line consists of 17 quadrupoles, arranged as two matching telescopes separated by 4 F0D0-cells with tunable phase advance.
For nominal settings the F0D0 cell will provide a betatron phase advance of $\mu_{x,y} = 45°$ per cell in both planes. Therefore four beam profile monitors separated by the same phase advance permit a fast emittance measurement based on the so-called multi-monitor technique [23] (see Section 4.2.3). Given the quadrupole spacing in the F0D0 channel L, the first telescope is used to match the Twiss parameters of the beam to the closed periodic solutions of the F0D0 channel, given by:

$$\beta^{\pm} = 2L\frac{1 \pm \sin\frac{\mu}{2}}{\sin\mu}, \tag{17}$$

where $\beta^{\pm}$ stands for the maximum (+) and minimum (-) value of the beta functions (which are achieved in the focusing and defocusing quadrupoles, respectively). The choice of L is a compromise between space charge forces, available length for the section and the minimum tolerable beam size. In order to measure the beam size with a high resolution and taking into account the presently achievable resolutions for the profile monitors, beam sizes in the F0D0 channel of the order of $100\,\mu$m are desirable. Space charge tends to prone smaller beam sizes (and shorter drifts between the quadrupoles) since the emittance over space charge ratio, as given by the rms envelope equation is:

$$\rho \simeq \frac{\gamma\sqrt{2\pi}\varepsilon\sigma_s}{2N_e r_e}\frac{2}{\langle\beta\rangle}, \tag{18}$$

where a cylindrical symmetric beam is assumed. $\langle\beta\rangle$ is the average beta function, r_e the classical radius of the electron, σ_s the rms bunch length and N_e the number of electrons per bunch. An illustration of the space charge evolution for different quadrupole spacings is presented in Fig. 18. A good compromise leads to a quadrupole spacing of 0.90 m; the desired phase advance of $\mu_{x,y} = 45\,°$ is achieved with an absolute value of the quadrupole strength of $|k_1| = 2.33\,\mathrm{m}^{-2}$.
The downstream quadrupole telescope is used to match the beam to the accelerator module, matching conditions are optimized after simulations of the downstream linac [12]. The optimized optical functions along the bunch compressor and diagnostic section are presented in Fig. 19. Taking into account space charge forces results in an emittance oscillation in the F0D0 channel (see Fig. 18) and some betatron beating. In the present design ($L = 0.9$ m) the relative emittance oscillation is below 10% peak-to-peak. However, the relative emittance growth between the entrance and exit of the F0D0 channel is less that 3%. Moreover it should be noted, that the results presented in Fig. 18 assume an emittance of 0.5 mrad mm, a larger emittance will decrease the sensitivity to space charge.

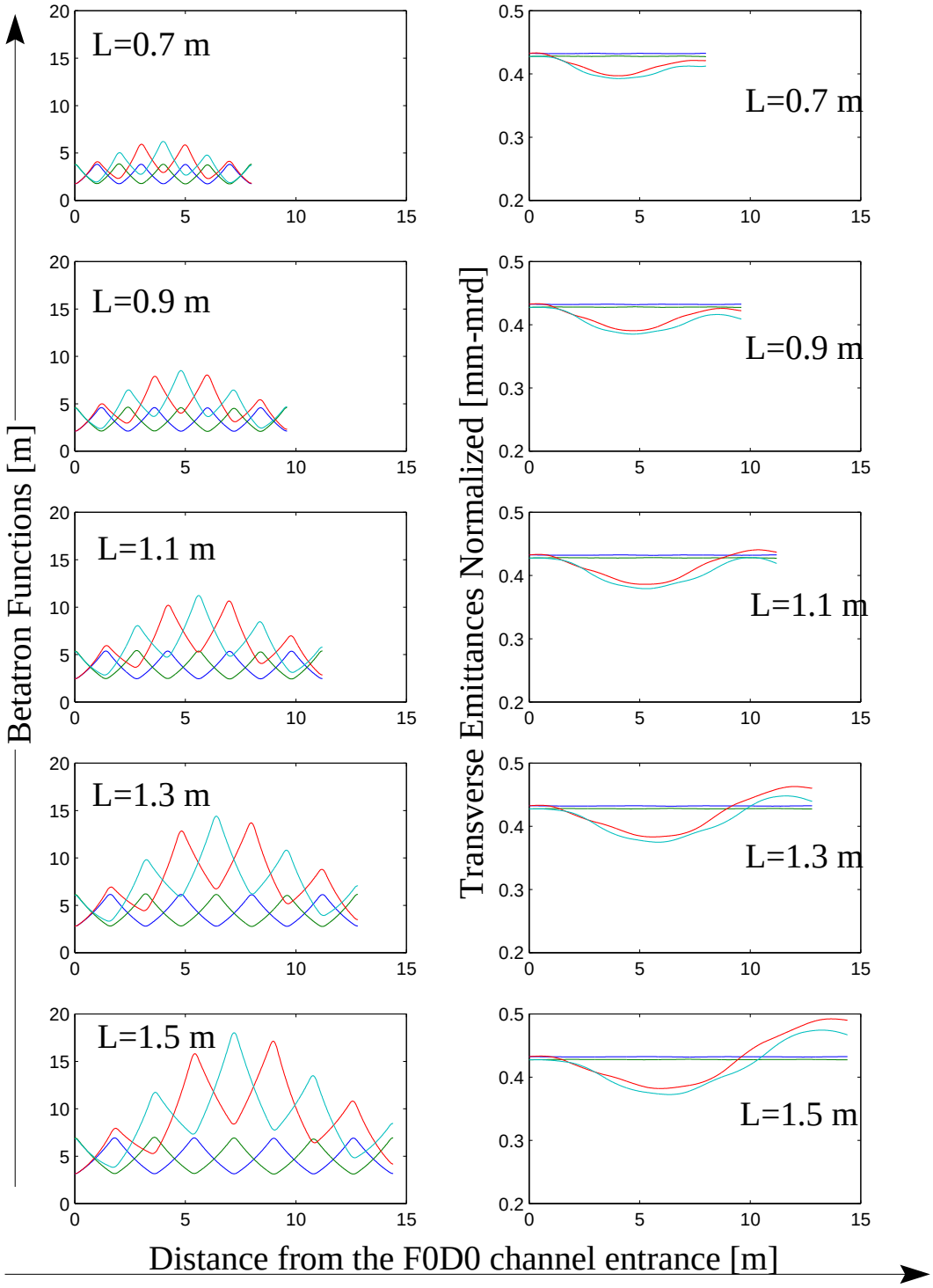

Figure 18: Comparison of calculated beta functions and emittances without space charge (blue and green curves) and with space charge (red and cyan curves).

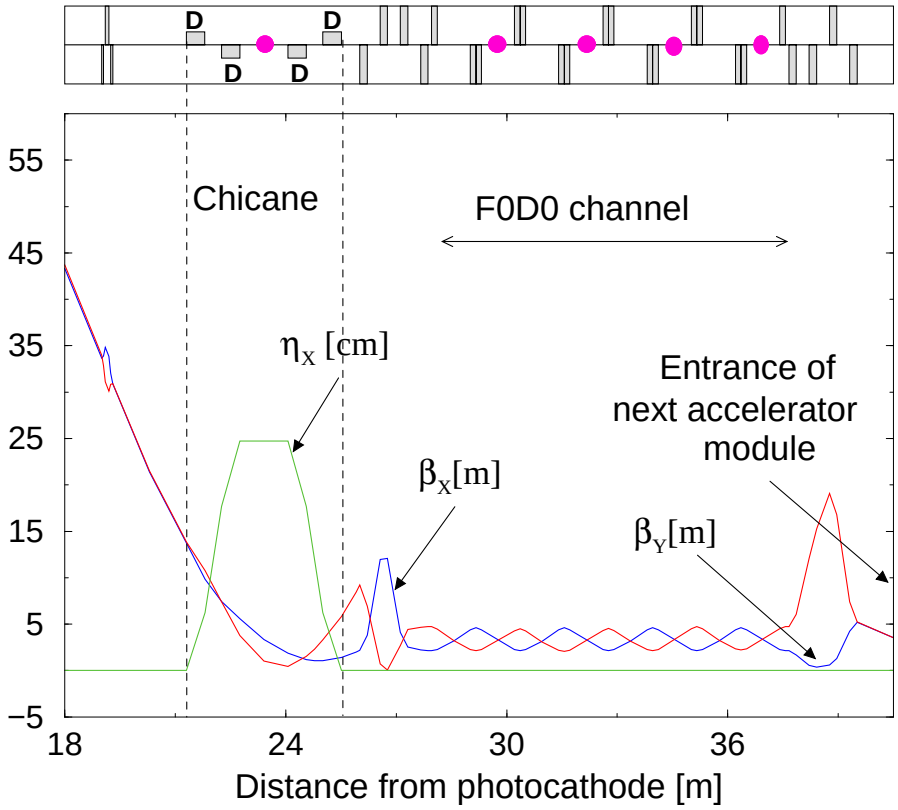

Figure 19: Optical lattice functions along the compressor and matching/diagnostic section. The dipoles and quadrupoles are indicated by rectangular boxes (D: dipole) and beam profile monitors by magenta bullets in the upper plot.

3 Tolerance studies

In a series of sensitivity runs using ASTRA and HOMDYN the requirements on the parameter stability of components with significant impact on the beam parameters (transverse emittance, bunch length and energy spread) have been studied. The results of these simulations are shown in Fig. 20 through Fig. 31. A compilation of the data is given in Table 5. The stability requirements should not be confused with the requirements on the absolute accuracy of the parameter setting which is significantly lower. A gradient differing from the nominal gradient in the gun cavity for example will require a somewhat different setting of the solenoid in order to achieve a small emittance. (For a similar injector configuration (the TTF2 injector) an emittance of $\simeq$1.4 mrad mm has been achieved with a gradient of only 40 MV/m in the RF gun.) The plots show the variation of the beam parameters for the case that a single parameter setting is drifting or shows some jitter.
The most challenging requirement is the amplitude stability of the RF gun, which has however been reached at the TTF RF gun [27]. The requirements on the amplitude and phase stability of the cavities in the module are on the other hand relaxed. A more stringent requirement of $\sim 1^\circ$ phase stability for the vector sum of all cavities of the module is required for the bunch compressor operation and is achieved by the TTF RF regulation system. The gradient and phase of individual cavities might however show larger variations.

Element	parameter	nominal value	tolerance	unit
laser	σ_r	0.75	$\pm$0.05	mm
	L_t	20.0	$\pm$1.0	ps
	q (charge or laser intensity)	1.0	$\pm$10%	-
gun	E_o	60	$\pm$0.3	MV/m
	ϕ	44	$\pm$2	$^\circ$
solenoid	$\hat{B}$	198	$\pm$1	mT
cavities 1 $\rightarrow$ 4	E	11.5	$\pm$1	MV/m
		-16.38	$\pm$5	$^\circ$
cavities 5 $\rightarrow$ 8	$\hat{E}$	25	$\pm$2.5	MV/m
	ϕ	-16.38	$\pm$5	$^\circ$
Third Harm.	E	13.9	$\pm$0.5	MV/m
	ϕ	-179.3	$\pm$2	$^\circ$

Table 5: Stability requirements of parameter settings of various beam line elements.

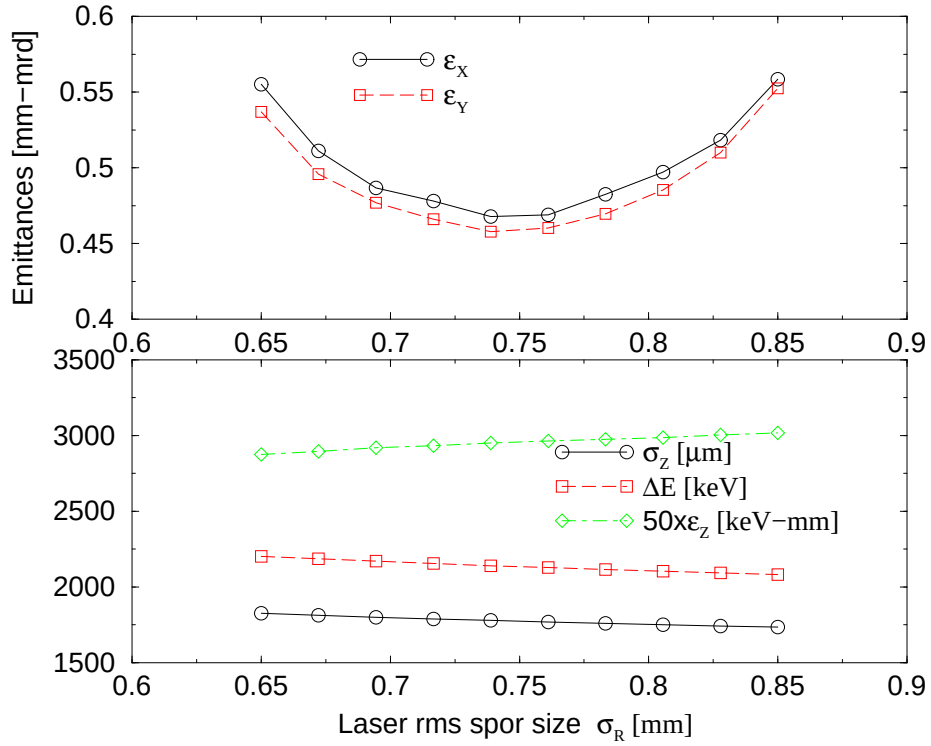

Figure 20: Sensitivity of transverse (top) and longitudinal parameters (bottom) to the rms spot size of the laser on the photocathode. The nominal setting is 0.75 mm. The parameters are calculated at z =18 m.

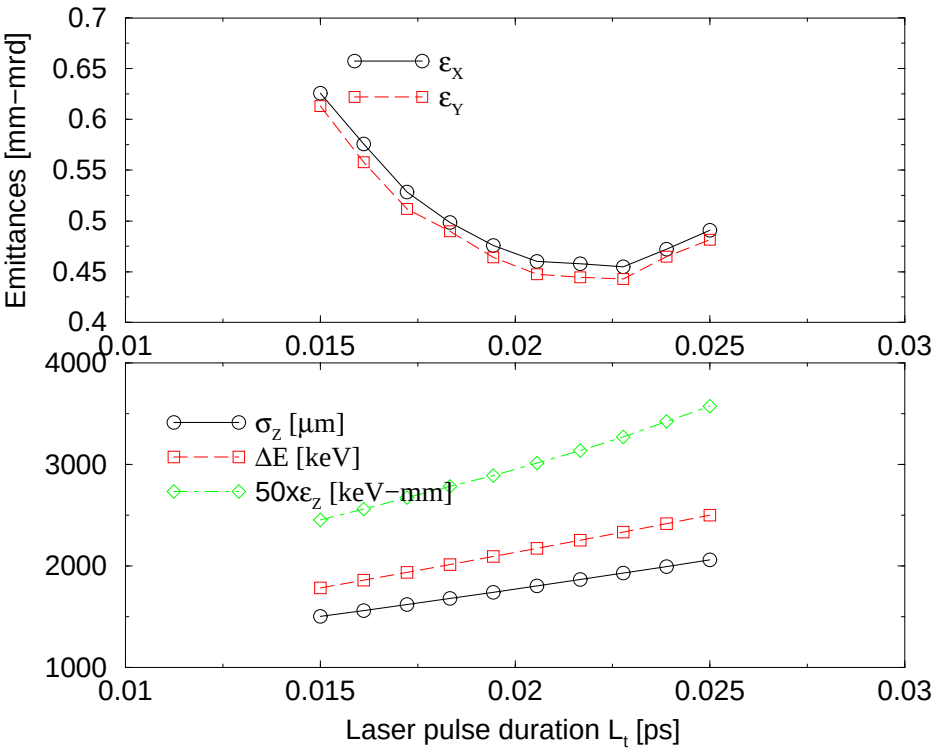

Figure 21: Sensitivity of transverse (top) and longitudinal parameters (bottom) to the pulse length of the laser on the photocathode. The nominal setting is 20 ps. The parameters are calculated at z =18 m.

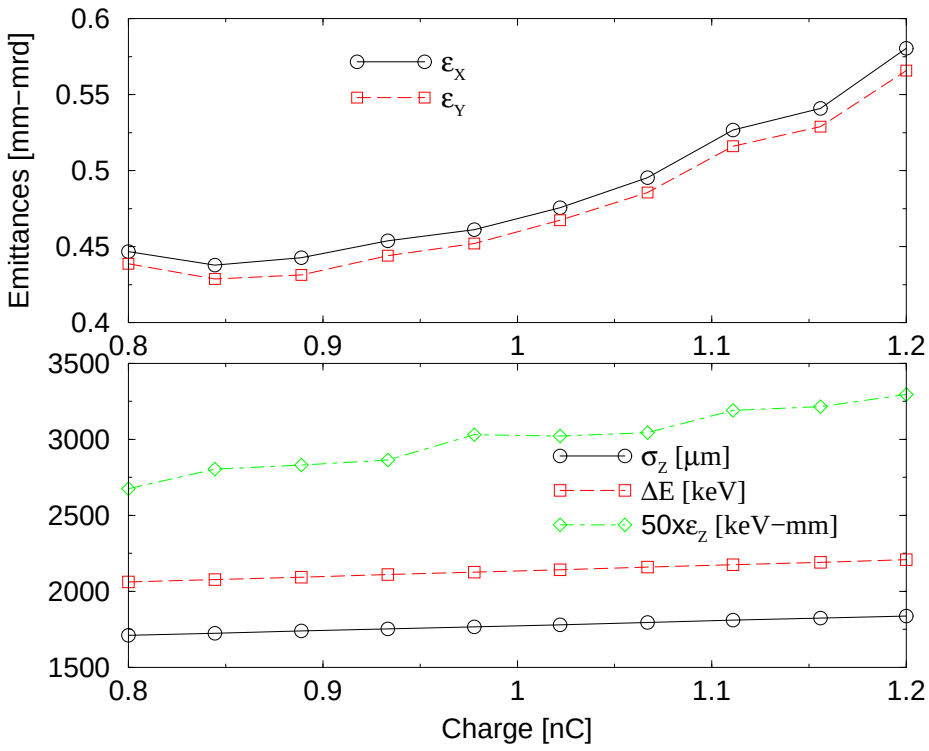

Figure 22: Sensitivity of transverse (top) and longitudinal parameters (bottom) to the bunch charge or the laser intensity. The nominal setting is 1.0 nC. The parameters are calculated at z =18 m.

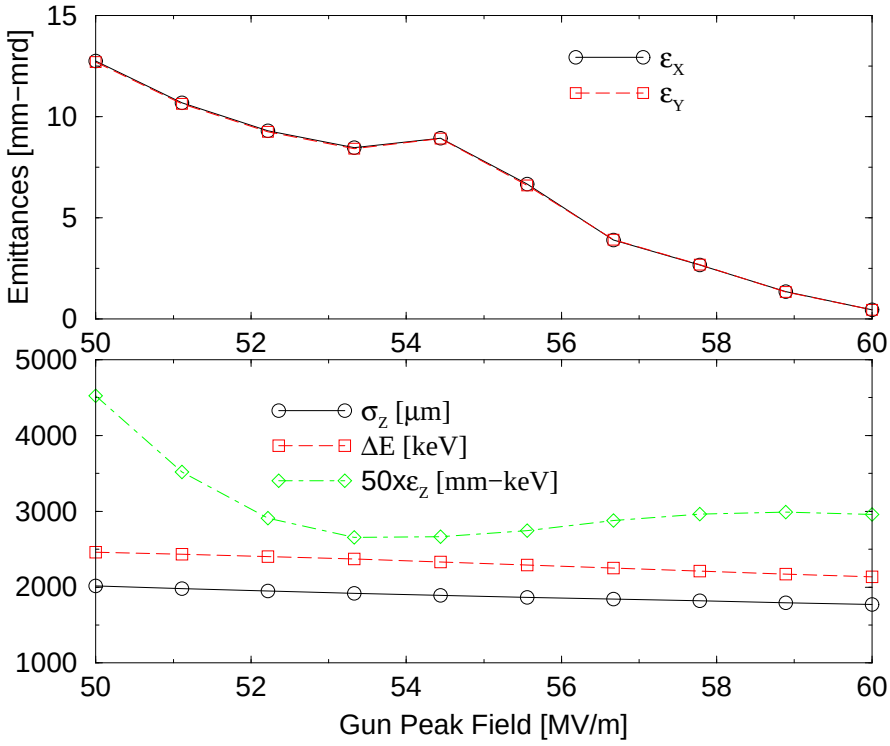

Figure 23: Sensitivity of transverse (top) and longitudinal parameters (bottom) on the peak field in the gun. The nominal setting is 60.00 MV/m. The parameters are calculated at z =18 m.

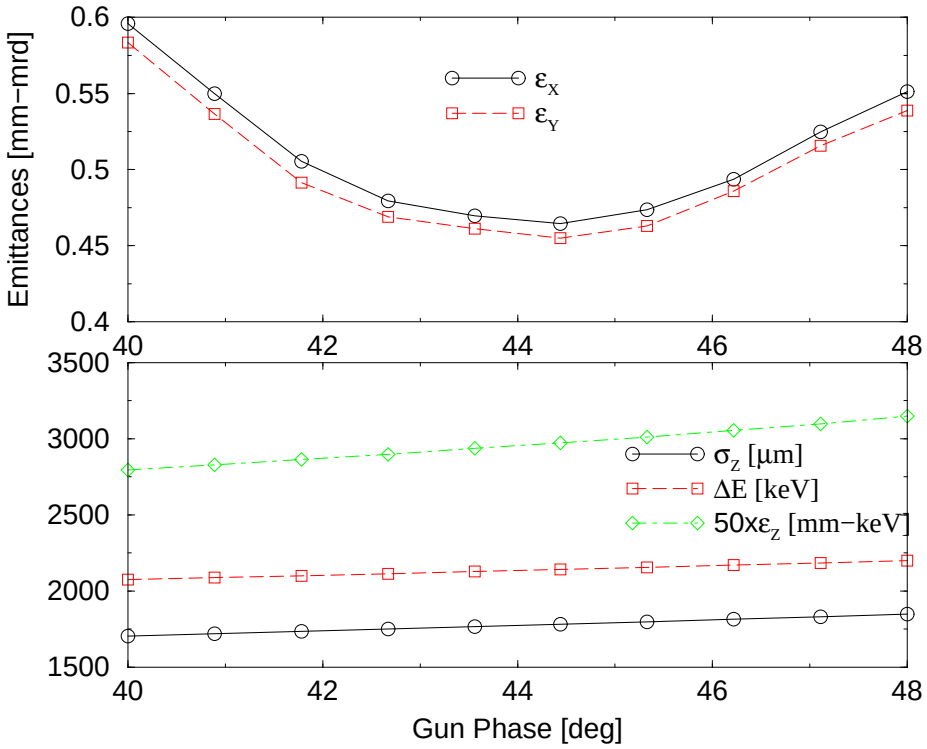

Figure 24: Sensitivity of transverse (top) and longitudinal parameters (bottom) on the gun phase. The nominal setting is 44.00°. The parameters are calculated at z =18 m.

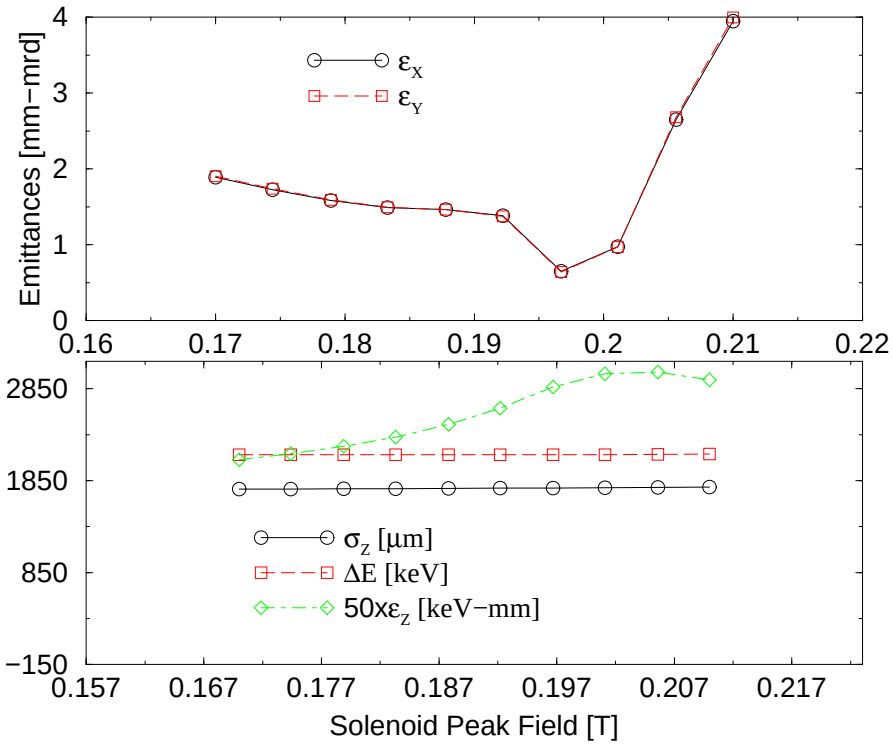

Figure 25: Sensitivity of transverse (top) and longitudinal parameters (bottom) to the strength of the gun solenoid. The nominal setting is 0.198 T. The parameters are calculated at z =18 m.

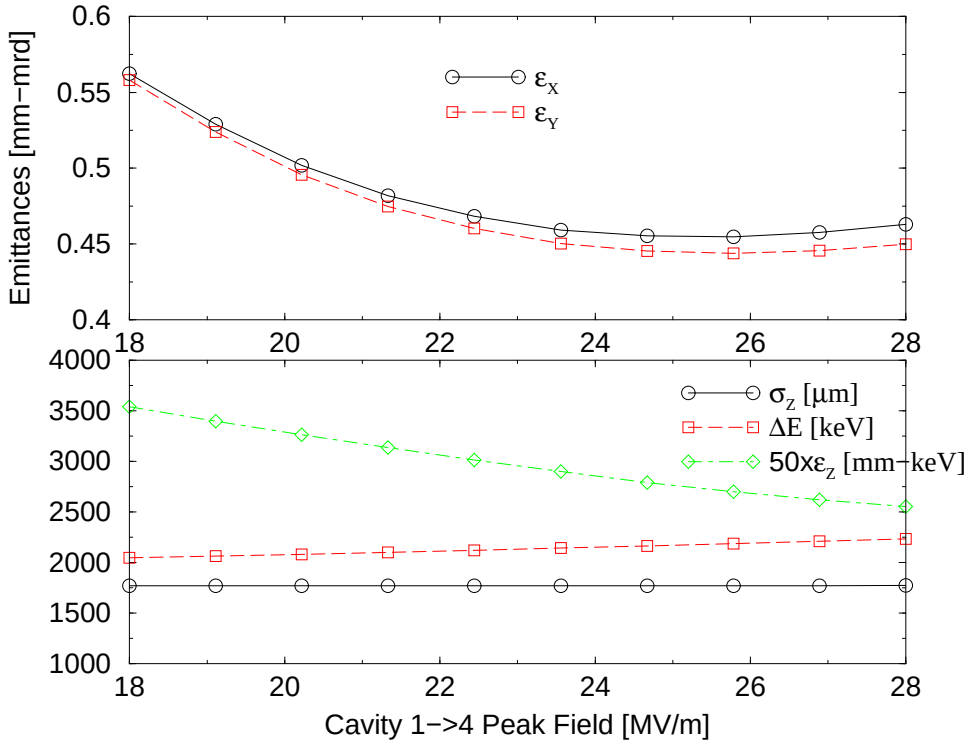

Figure 26: Sensitivity of transverse (top) and longitudinal parameters (bottom) to the peak field of cavity #1 through #4. The nominal setting is 23.00 MV/m, corresponding to an average field of 11.5 MV/m. The parameters are calculated at z =18 m.

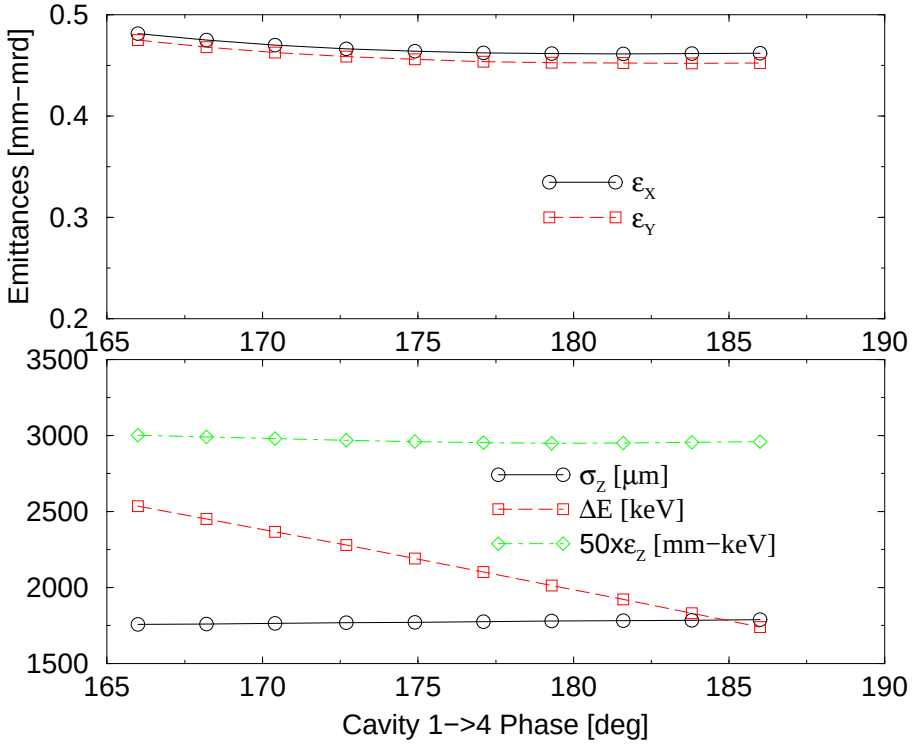

Figure 27: Sensitivity of transverse (top) and longitudinal parameters (bottom) to the RF phase of cavity #1 through #4. The nominal setting is 176.33°. The parameters are calculated at z =18 m.

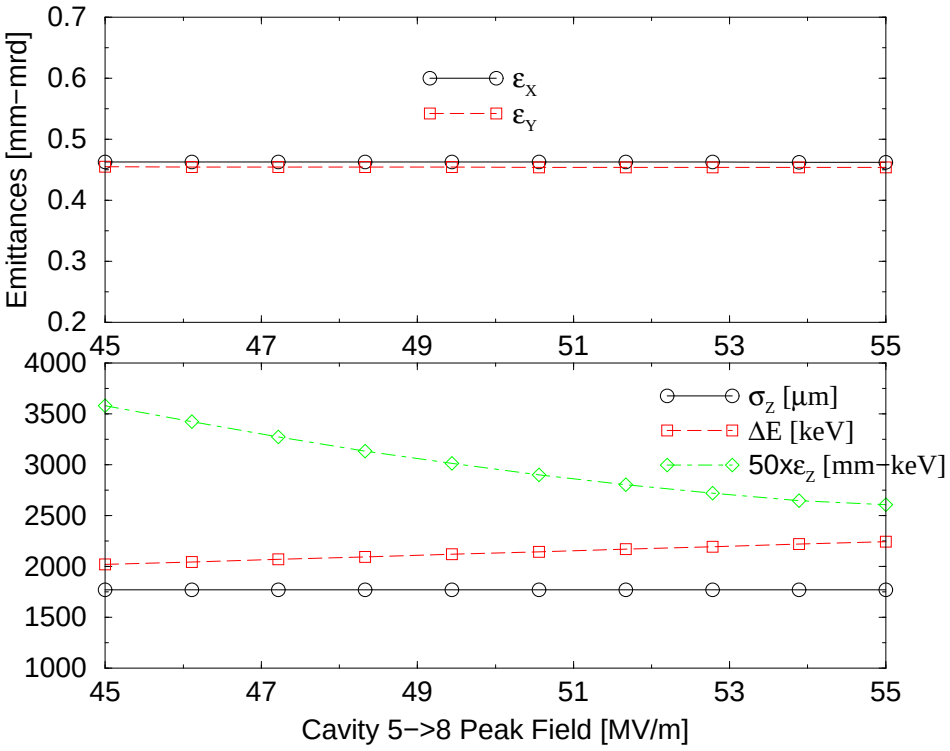

Figure 28: Sensitivity of transverse (top) and longitudinal parameters (bottom) to the peak field of cavity #5 through #8. The nominal setting is 50.00 MV/m, corresponding to an average field of 25 MV/m. The parameters are calculated at z =18 m.

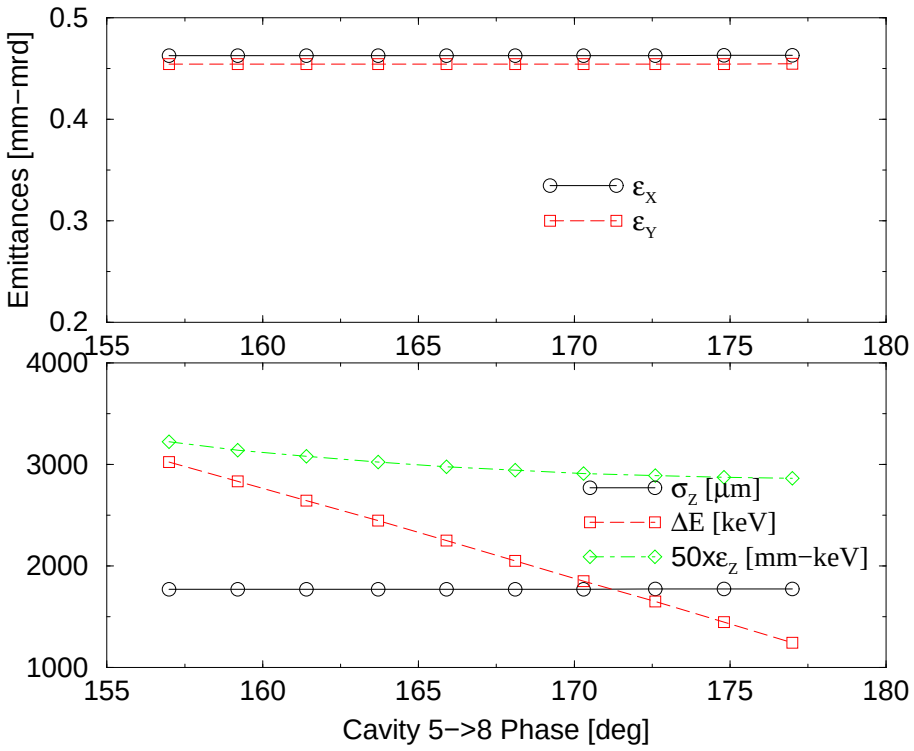

Figure 29: Sensitivity of transverse (top) and longitudinal parameters (bottom) to the RF phase of cavity #5 through #8. The nominal setting is 167.21°. The parameters are calculated at z =18 m.

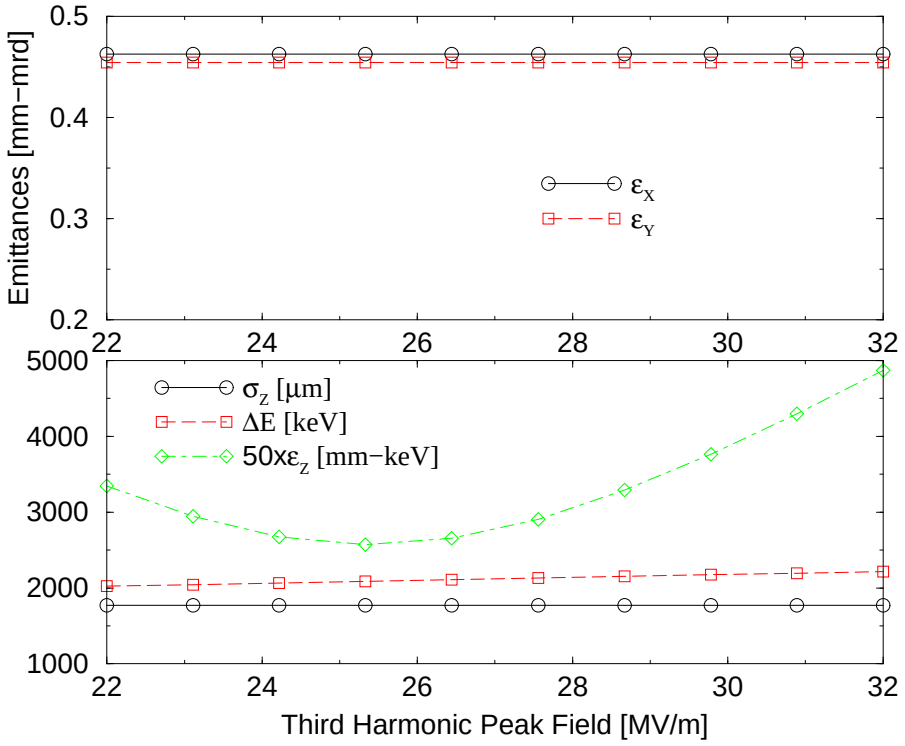

Figure 30: Sensitivity of transverse (top) and longitudinal parameters (bottom) to the peak field of the third harmonic section. The nominal setting is 27.72 MV/m, corresponding to an average field of 13.9 MV/m). The parameters are calculated at z =18 m.

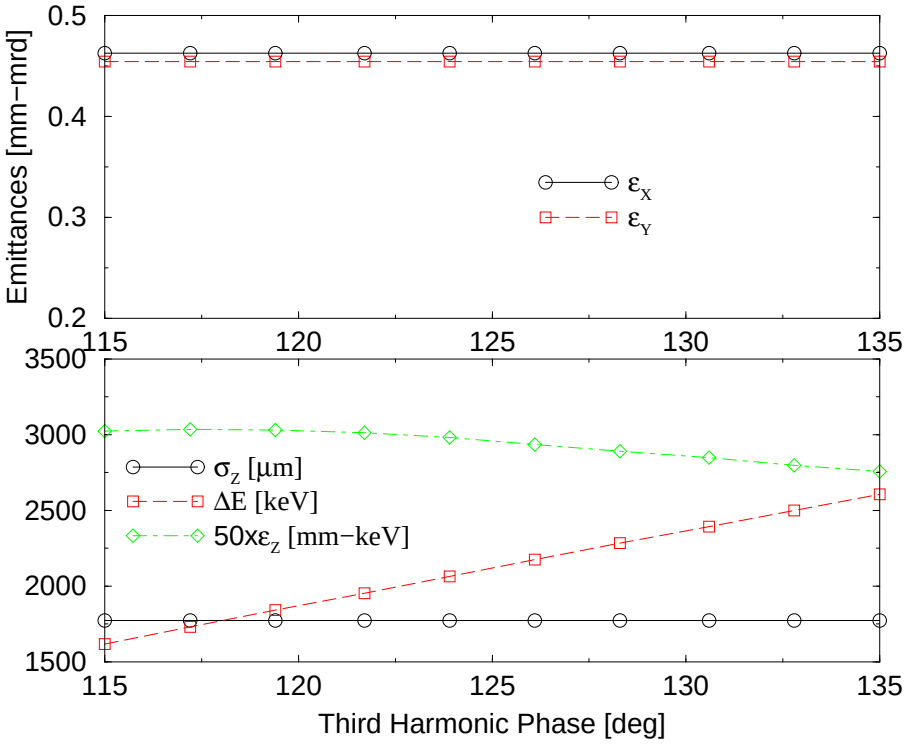

Figure 31: Sensitivity of transverse (top) and longitudinal parameters (bottom) to the RF phase of the third harmonic section. The nominal setting is 125.28°. The parameters are calculated at z =18 m.

4 Diagnostics Section

Beam diagnostics in the injector is a crucial point, since adjustable parameters of all beam line components have to be experimentally optimized. The calculated parameters are the starting point for the operation, but will require some fine tuning. A full characterization of the beam parameters during commissioning is required in order to verify that the beam properties are as expected. It is however also important to forsee simple diagnostics to monitor (fast and possibly non-interceptive) some beam parameters or typical signatures which can help to identify drifts in the system during standard operation.

4.1 Charge Measurement

A Faraday cup inserted between gun and booster allows an absolute charge measurement, while toroidal AC transformers are used to monitor the charge along the beam line and to detect beam losses. Four toroids are foreseen for the injector: (1) upstream and (2) downstream of the first accelerator module, (3) downstream of the compressor chicane and (4) in front of the second accelerating section.

4.2 Transverse Diagnostics

4.2.1 Beam Position Measurement

The beam position must be known in order to steer the beam onto an ideal orbit and to measure the transverse transfer functions of the lattice. In the FEL-injector the beam position will be measured with electro-magnetic pickups.

4.2.2 Transverse Beam Profile Measurement

The beam distribution is determined by means of observation screens. At low energy, i.e. directly downstream of the RF gun, Yttrium:Aluminum:Garnet (YAG) screens are suitable due to their high electron-to-photon conversion efficiency. Downstream of the booster section optical transition radiation (OTR) screens will be used. This screens consists of Aluminum mirrors which are inserted into the beam. If the mirror is inserted with a 45° angle, the backward transition radiation is emitted at 90° w.r.t. the beam direction and collected by an optical system.[4] The images will be recorded with CCD cameras. With a single lens optics a resolution of 10 μm can be achieved [30, 31]. In the bunch compressor area, synchrotron radiation in the optical regime (the critical wavelength is $\simeq$ 300 nm), permits non-interceptive

[4] To reduce the depth of field aberration inherent to the 45° configuration, it is possible to use the forward transition radiation along with an extraction mirror as in Ref. [29].

measurements of the transverse density both at high (second and third dipole) and low (first and fourth dipole) dispersion points.

4.2.3 Transverse Projected Emittance Measurement

The transverse projected emittance will be measured with two different techniques: (1) the so-called quadrupole scan and (2) the multi-monitor method.

Quadrupole Scan The quadrupole scan is an indirect method for emittance measurements based on an envelope fitting technique. The transfer matrix between a measurement position, i.e. a location where the Twiss parameters and emittance should be measured, and an observation point, i.e. a location instrumented with a transverse profile monitor is varied and the spot size is recorded. The transfer matrix can be varied in different ways, for instance by a single or by several quadrupoles. In the following the simplest case of a single quadrupole, which can be scanned monotonically, so that no hysteresis cycling is required during the measurement, is analyzed.
In order to achieve a precise measurement, the upstream lattice has to be optimized. Assuming that the quadrupole can be approximated as a thin lens, the transfer matrix M between the quadrupole entrance (the measurement position) and the observation point writes as:

$$M = \begin{pmatrix} R_{11} & R_{12} \\ R_{21} & R_{22} \end{pmatrix} \begin{pmatrix} 1 & 0 \\ k_1 l & 1 \end{pmatrix}, \tag{19}$$

where k_1 and l are the quadrupole strength and length. The transport between the quadrupole exit and the observation point may be described by a simple drift matrix, but may also contain quadrupoles in order to improve the accuracy of the method.
The beta function at the observation point takes the form:

$$\beta_o = \beta_Q (R_{11} + k_1 l R_{12})^2 - 2\alpha_Q (R_{11} + k_1 l R_{12}) R_{12} + \frac{1 + \alpha_Q^2}{\beta_Q} R_{12}^2, \tag{20}$$

where $_Q$ stands for the Twiss parameters at the quadrupole entrance. For a high accuracy it is required, that the minimal possible spot size at the observation point, i.e. when the waist is at the screen position, is determined. It is desirable to achieve a beam waist in both planes on the observation screen for an unexcited quadrupole. This ensures, that the waist is covered (in both planes) within the scanning range of the quadrupole and has the additional advantage that the spot is round during the scan, which avoids problems with the read-out system. (Highly elliptical beams tend to produce more problems with saturation and resolution limits of the screen and the CCD camera.)
With a waist for an unexcited quadrupole ($d\beta/dk_1 = 0$ for $k_1 = 0$) the relation between the Twiss parameters at the quadrupole entrance is:

$$\frac{\alpha_Q}{\beta_Q} = \frac{R_{11}}{R_{12}} \tag{21}$$

When this equation is satisfied the beta and alpha functions at the observation point take the form:

$$\beta_o = \frac{R_{12}^2}{\beta_Q} \tag{22}$$

So given a desired minimum beam spot (β_o) during a quadrupole scan, the required α_Q and β_Q can be determined using Eq. (21) and (22). A set of four quadrupoles upstream of the scanning quadrupole is required to fit the lattice functions to the desired values in both transverse planes. In practice an iterative procedure will be required to optimize the settings. A simulation of a quadrupole scan is presented in Fig. 33 and Fig. 34, for two cases of incoming beta functions. It is assumed, that the beam spot is observed on the second screen in the F0D0 channel and the next but first upstream quadrupole is scanned as sketched in Fig. 32. In the "high-β" case, the beta function at the quadrupole entrance is 5 m. This large beta function results in a minimum beam spot of about 50 μm. Reducing the beta function at the quadrupole entrance to 1 m results in a minimum beam spot of 100 μm. A fitting algorithm is applied to determine the emittance. The simulation of the measurement is presented in Fig. 34 for the two cases of beta functions as a function of the beam profile monitor resolution. The simulation includes an error propagation algorithm, which takes the resolution of the profile monitor and a statistical error on the rms beam size measurement into account. The simulation has been performed for two different statistical errors on the rms beam size of 10 and 50 μm. Comparing the two results clearly shows the advantages of the low-beta case: First a worse resolution can be tolerated: typically 30 μm should be sufficient to resolve the emittance with a 10% error. Secondly smaller error bars in the low-beta case indicate a reduced sensitivity to statistical errors on the beam size measurement.

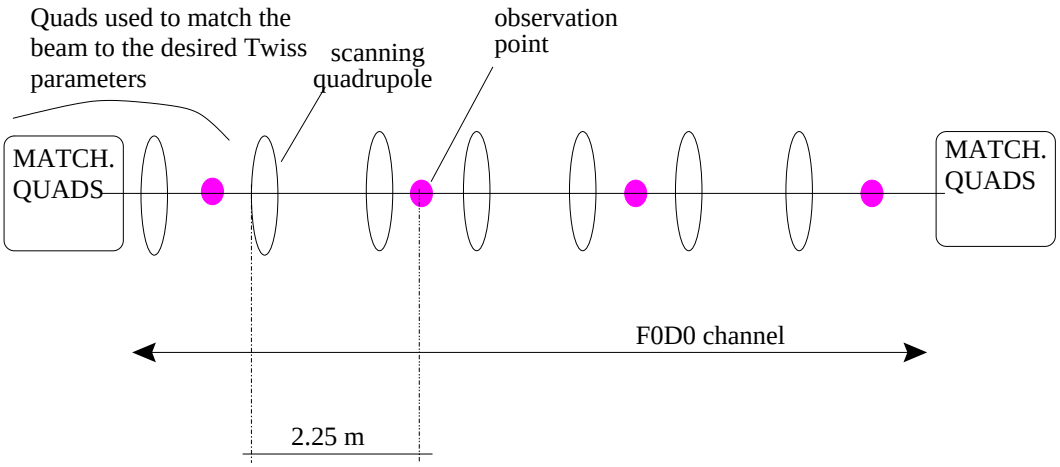

Figure 32: Schematic set-up for the quadrupole scan simulations at the XFEL injector.

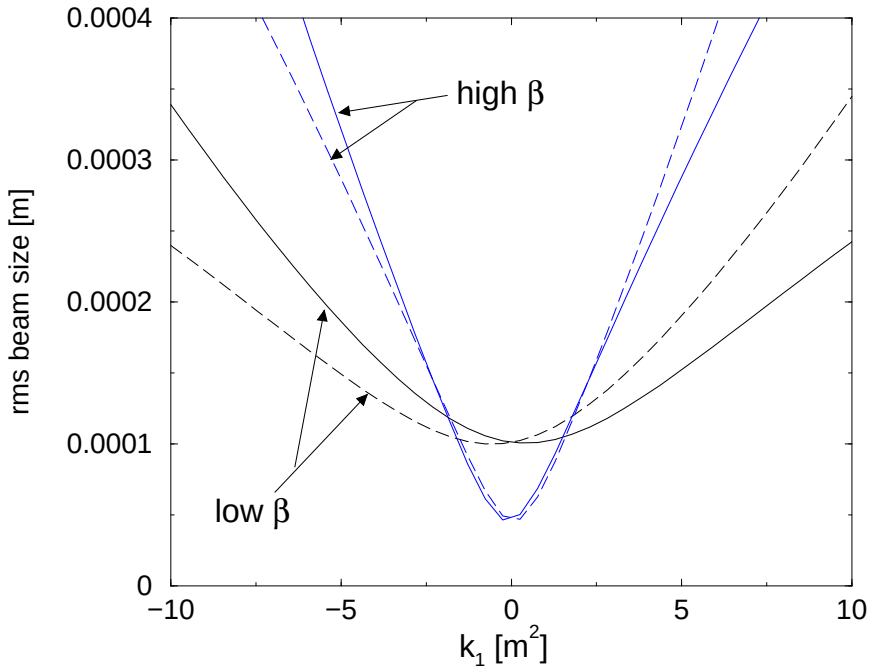

Figure 33: A quadrupole scan for two incoming (α, β) couples at the quadrupole entrance. The variation of the horizontal (solid lines) and the vertical (dashed lines) beam size versus the excitation of an upstream quadrupole in the F0D0 channel is plotted. Low β: $\alpha_Q = 0.45$, $\beta_Q = 1.00\,\mathrm{m}$. High β: $\alpha_Q = 2.25$, $\beta_Q = 5.00\,\mathrm{m}$.

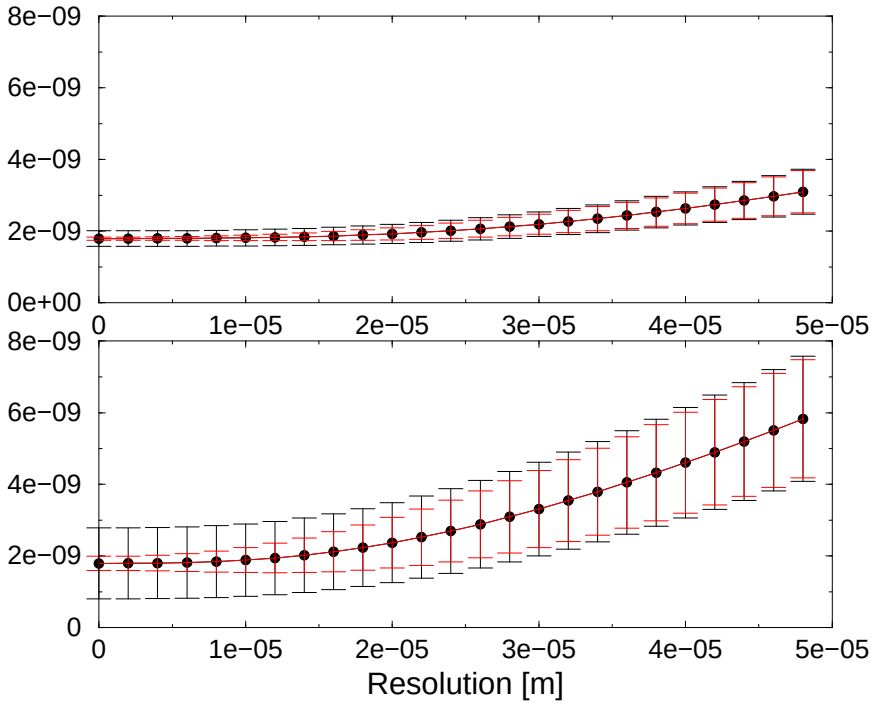

Figure 34: Simulation of the emittance measurement from the data presented in Fig. 33. The vertical axis is the "measured" emittance after the simulation of the measurement. The nominal geometrical emittance is $1.8{\cdot}10^{-3}$ mrad mm. The top and bottom plots correspond to the "low-" and "high-beta" cases in Fig. 33, respectively. For each case the simulation was performed with a 10 μm (smaller error bars) and 50 μm statistical error on the rms beam size measurement.

Multi-monitor Technique For the second method the beam size at different locations along the beam line is measured. The betatron phase advance between the observation points is crucial: it should be chosen to sample one half a betatron period as well as possible. In Fig. 35 and Fig. 36 simulations of a measurement are presented for two cases: A lattice with four monitors separated by 45° and a lattice with three monitors separated by 60°. Using four monitors separated by 45° instead of the three monitors with 60° phase advance strictly needed to determine the three independent parameters ϵ, α and β, provides information about the measurement error of the calculated emittance. The measurement simulations are performed by computing the horizontal and vertical beam size at the location of the profile monitors from distributions generated with ASTRA and tracked with ELEGANT. The emittance is approximately 0.5 mrad mm (i.e. $\simeq 1.8{\cdot}10^{-3}$ mrad mm geometrical) so that the average beam size is about is 80 μm (rms) in both planes. For the simulation this is a pessimistic assumption, since the thermal emittance along with emittance dilution in front of the F0D0 channel will contribute to an increased emittance of $\simeq$1 mrad mm. In addition to the resolution limit of the beam size monitor a spot size jitter of 10μm is assumed. The resolution requirement is higher in case of the multi-monitor method, as compared to the quadrupole scanning technique, thus it tends to be less precise, but it provides an almost on-line measurement without any optics tune-up; thus it is well suited for regular checking and tuning.

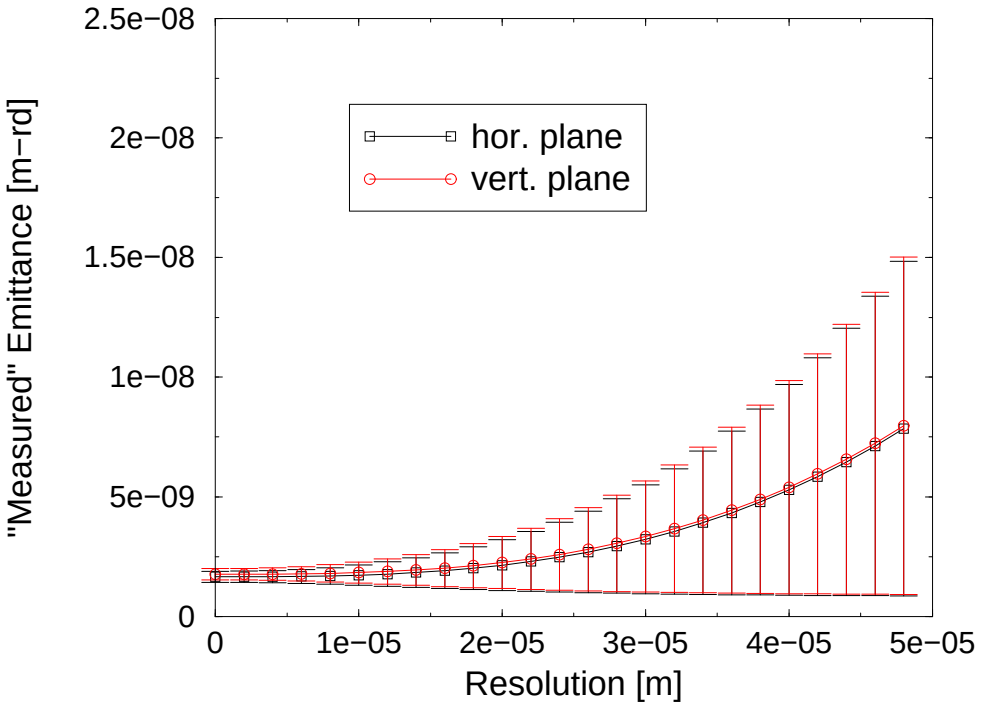

Figure 35: Simulation of the emittance measurement with the multi-monitor technique in a 45° lattice. The nominal geometrical emittance is $1.8{\cdot}10^{-3}$ mrad mm. The statistical error on the rms beam size measurement is assumed to be 10 μm.

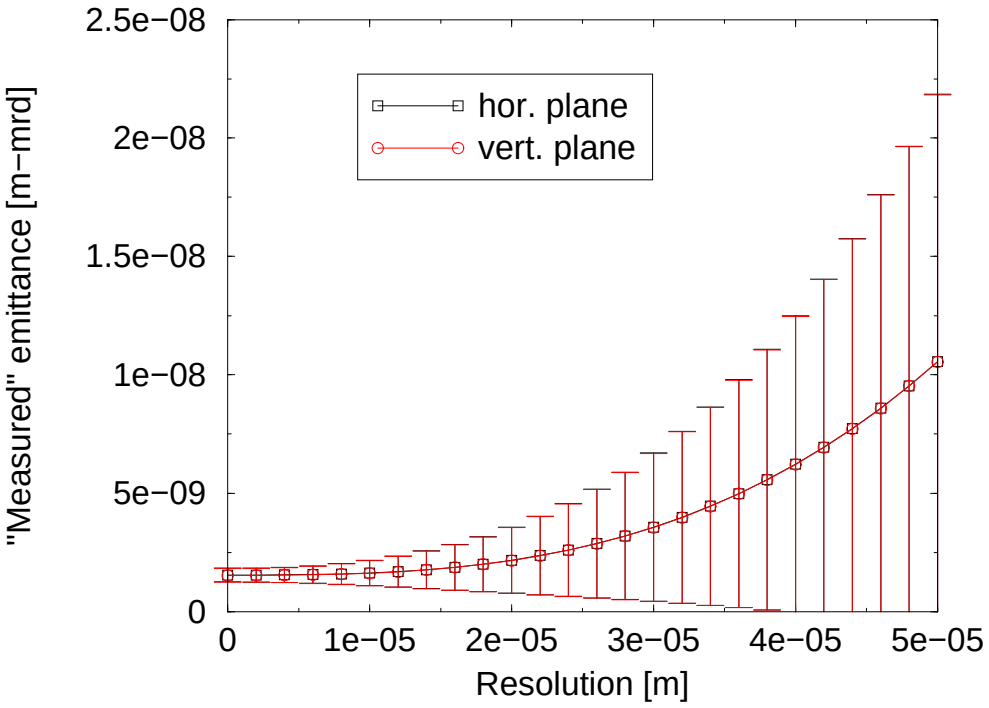

Figure 36: Simulation of the emittance measurement with the multi-monitor technique in a 60° lattice. The nominal geometrical emittance is $1.8{\cdot}10^{-3}$ mrad mm. The statistical error on the rms beam size measurement is assumed to be $10\,\mu$m.

4.2.4 Transverse Slice Emittance Measurement

The measurement of the slice emittance is possible by cutting a slice out of the bunch in the dispersive section of the bunch compressor with a slit with variable width and position and analyzing it downstream with the quadrupole scan or the multi-monitor method. A linearly correlated energy spread, which is introduced by operating the accelerating cavities off-crest transforms into a linear correlation between longitudinal position within the bunch and transverse off-set. The introduced non linearities are independent of the way in which the energy spread is introduced, i.e. operating a single cavity far off-crest or by a number of cavities only somewhat off-crest. They can be compensated by the third harmonic section if required. The transverse off-set in the dispersive section can be written as:

$$\Delta x(s) = \eta \frac{\Delta p}{p} \frac{s}{\sigma_s} \ , \tag{23}$$

where $\frac{\Delta p}{p}$ is the correlated momentum spread, η is the dispersion and s and σ_s refer to the position in the bunch and the rms bunch length in front of the bunch compressor, respectively. The contribution of the beam emittance to the spot size is small at this point and has been ignored here. For nominal settings with $\simeq$1.5% energy spread, η=0.25 m and σ_s=1.7 mm a slit width of 1 mm corresponds to a longitudinal slice of $\simeq$0.5 mm. Shorter slices require a smaller slit width or a larger momentum spread.

4.3 Longitudinal Diagnostics

4.3.1 Energy and Energy Spread Measurement

A low energy ($\simeq$6 MeV) spectrometer between the gun and the accelerating module allows the measurement of the average and rms energy generated in the gun. Most of the energy related measurements are however foreseen to occur in the post-acceleration section since the incoming (correlated) energy spread has to be tuned to achieve the desired bunch length in the bunch compressor. The energy spread can be inferred by observing the beam in a dispersive section. The spot size is a convolution of the emittance contribution and the dispersive contribution and can to first order be written as: $\sigma_x \simeq \sqrt{\beta_x \tilde{\varepsilon}_x + \eta_x^2 \langle (\Delta p/p)^2 \rangle}$. Here $\tilde{\varepsilon}_x$ denotes the geometrical emittance. The spot size should be dominated by the dispersive term, so that $\beta_x \tilde{\varepsilon}_x \ll \eta_x^2 \langle (\Delta p/p)^2 \rangle$.
Beam profile measurements are foreseen at two locations with dispersion: (1) at the chicane mid-point and (2) in a spectrometer line described below.
At the chicane mid-point the horizontal dispersion is η=0.246 m for the nominal bending angle of 14.2°. For low emittance beams an energy spread measurement is possible without modifications of the nominal optics.
The fourth bend of the bunch compression chicane can be use to direct the beam into a spectrometer line as sketched in Fig. 37. It allows the measurement of energy spread when the chicane is operated (i.e. by simply switching the fourth dipole off – this mode

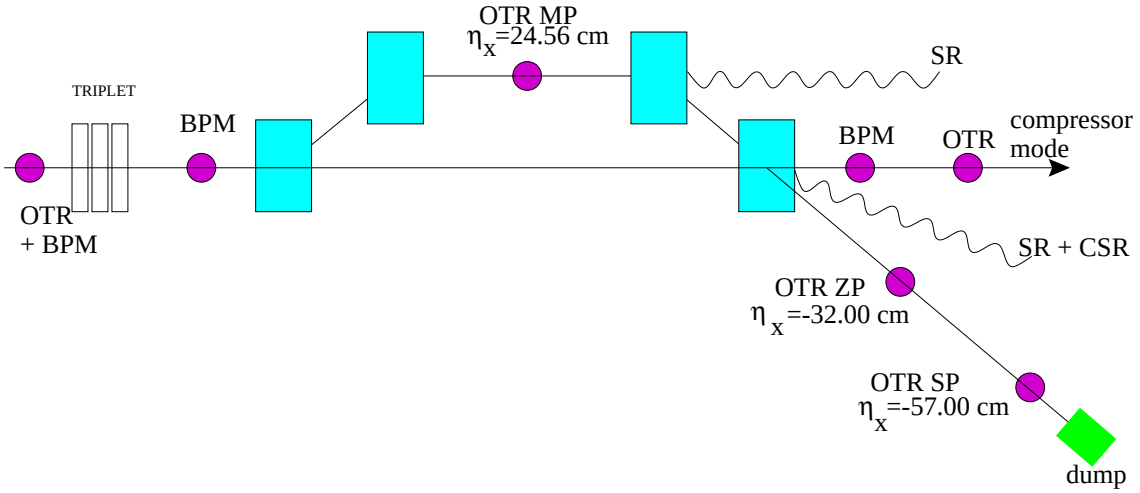

Figure 37: The bunch compressor and spectrometer line with its diagnostic stations.

is referred to as "compressor & spectrometer" in Table 6) and also when the chicane is bypassed (i.e. by exciting the fourth dipole to the opposite polarity – this mode is referred to as "spectrometer only" in Table 6). For the measurements in the spectrometer line the upstream triplet setting is modified in order to minimize the beat function at the screen location. Table 6 summarizes the measurement locations and achieved optical functions along with the expected resolution of the measurement. The rms resolutions presented in

Operating mode	dipole settings	OTR	β_x [m]	η_x [m]	resolution
compressor straight nominal[a)]	+/-/-/+	MP	3.46	-0.25	$\simeq 5 \cdot 10^{-4}$
compressor & spectrometer[b)]	+/-/-/0	SP	0.39	-0.57	$\simeq 1 \cdot 10^{-4}$
spectrometer only[b)]	0/0/0/-	SP	0.35	-0.57	$\simeq 1 \cdot 10^{-4}$

Table 6: Operating modes of the dispersive section, achieved beta and dispersion functions at the observation point and resolution limits for the different possibilities of energy spread measurements. **a)** the lattice functions are obtained with the nominal settings. **b)** the lattice functions are obtained after optimization of the optics.

the table are computed as $1/\eta_x \cdot \sqrt{\Sigma_x^2 + \beta_x \tilde{\varepsilon}/(\beta\gamma)}$ where Σ_x is the resolution of the profile monitor (assumed to be $50\,\mu$m), and the normalized emittance is taken to be 1 mrad mm. The high resolution ($\simeq 1 \cdot 10^{-4}$) provided by the profile measurement station in the spectrometer offers an excellent tool for observing and investigating potential sub-structures in the energy distribution.

4.3.2 Bunch length Measurements, Time Domain Techniques

The rms bunch length to be measured downstream of the compressor is expected to range from 2 mm ($\simeq$6.7 ps) when the compressor is off, to 270 μm ($\simeq$900 fs) for nominal compressor settings and down to 50 μm ($\simeq$170 fs) in case of complete compression.

Streak Camera Measurement The light from the OTR monitors located (1) in the spectrometer beam line and (2) downstream of the compressor and (3) the synchrotron radiation light from the fourth bunch compressor dipole is appropriate for streak camera measurements. A camera with 200 fs resolution [33] provides the bunch length and charge density distribution. The measurement of synchrotron radiation is non-interceptive and could thus be done during standard operation to check the accelerator stability. When the OTR monitor located in the spectrometer line is used, the streak direction should be vertical so that the streaked picture directly provides the longitudinal phase space [34]. The streak camera can measure only the uncompressed bunch length or the bunch length when the compressor is operating under nominal conditions. However, it might be required, e.g. during commissioning, to generate the shortest bunch length possible using the first bunch compressor, in this case the bunch length has to be measured downstream of the next accelerating section in a spectrometer by means of the so-called zero-phasing technique [35] since the required resolution is below the (present) state-of-art streak camera capability.

Zero-Phasing Measurement For the zero-phasing technique [35] a part of an accelerating section is operated at one of the RF zero-crossing phases. Thus a time-energy correlation will be induced and the observation of the energy profile (i.e. in a dispersive section) will be representative for the bunch charge density. The beam size at the observation point can be written as:

$$\langle x_{\pm}^2 \rangle = \langle x_{\beta}^2 \rangle + \eta^2 \langle \delta^2 \rangle = \langle x_{\beta}^2 \rangle + (C_1 \pm C_o)^2 \langle s^2 \rangle, \tag{24}$$

where no correlation between the transverse and longitudinal phase space is assumed. The sign $\pm$ accounts for the two possible zero-crossing points. C_o and C_1 have the same definitions as in Reference [35]: $C_o = \frac{\eta}{E_o}\frac{2\pi V_{rf}}{\lambda_{rf}}$ and $C_1 = \frac{\eta}{E_o}\frac{dE}{ds}$, where V_{rf} is the total accelerating voltage of the zero-phased section, E_o is the beam energy, η the dispersion at the observation point and dE/ds is the longitudinal phase space slope of the incoming beam. The bunch length can be calculated from measurements of the rms quantities: $\langle x_+^2 \rangle^{1/2}$, $\langle x_-^2 \rangle^{1/2}$, and $\langle x_o^2 \rangle^{1/2}$ (the latter is the beam size at the observation point with the zero-phasing cavities turned off):

$$\langle s^2 \rangle = \frac{\langle x_+^2 \rangle + \langle x_-^2 \rangle - 2\langle x_0^2 \rangle}{2C_o^2}. \tag{25}$$

Note that Eq. (25) is different from Reference [35] since the incoming energy spread of the bunch compared to the energy spread generated by the zero-phasing cavity(ies) cannot be

neglected. The incoming longitudinal phase space slope can also be estimated from the coefficient C_1:

$$\frac{dE}{ds} = \frac{E_o}{\eta}\frac{C_o}{2}\frac{\langle x_+^2\rangle - \langle x_+^2\rangle}{\langle x_+^2\rangle + \langle x_-^2\rangle - 2\langle x_0^2\rangle}, \tag{26}$$

A simulation for an uncompressed bunch is shown in Fig. 38: The beam spot is observed on the screen noted ZC in Fig. 37. In this example only one cavity is used to introduce the z-δ correlation. The voltage of the cavity is 27 MV, the dispersion at the observation point is $\eta_x \simeq$-32 cm and the incoming energy is 113 MeV. The rms beam sizes $\langle x_+^2\rangle^{1/2}$, $\langle x_-^2\rangle^{1/2}$ and $\langle x_o^2\rangle^{1/2}$ are 8.6, 1.5, and 5.0 mm, respectively. Using Eq. (25) the bunch length is calculated as 1.73 mm; in excellent agreement with the bunch length in the simulation at z =18 m of σ_s =1.77 mm. The same method could be used at the second bunch compressor for measuring the bunch length after compression in the first compressor. In this case several cavities of the next accelerator module would be needed to introduce the z-δ correlation.

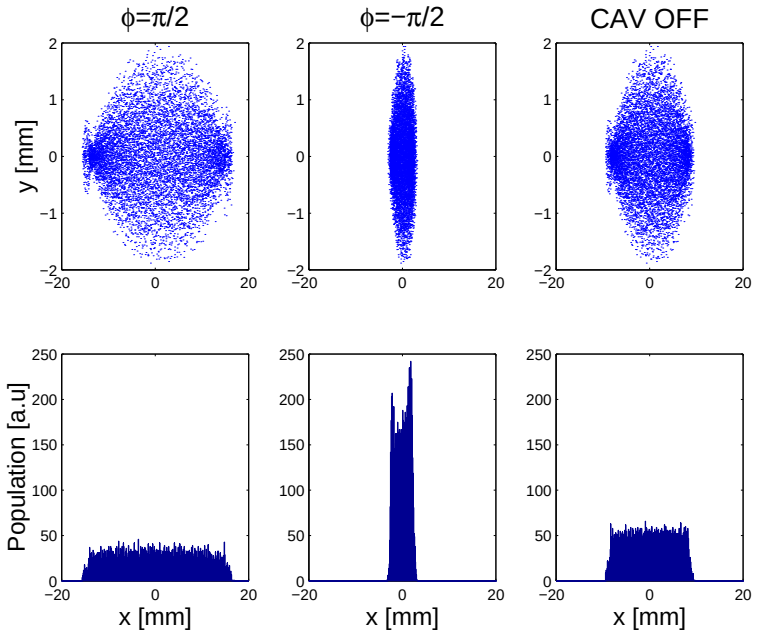

Figure 38: Beam spots and horizontal (dispersed) profiles expected during a bunch length measurement with the the zero-phasing method.

4.3.3 Bunch Length Measurements, Frequency Domain Techniques

Bunch length measurements based on frequency domain techniques have evoked growing interest in recent years. All methods consists of detecting radiation emitted by the electron bunch. Since electrons in a bunch are randomly distributed, wavelength smaller that a characteristic bunch length don't provide information on the longitudinal bunch distribution. Thus the radiation is detected at wavelength $\lambda \simeq \sigma_s$, i.e. in the coherence regime, where the power density radiated by a bunch of N electrons, $\left[\frac{dW}{d\Omega d\omega}\right]_{Ne}$, is related to the single electron radiated power, $\left[\frac{dW}{d\Omega d\omega}\right]_{1e}$, via (assuming the bunch is a line charge distribution, i.e ignoring transverse effects):

$$\left[\frac{d^2W}{d\Omega d\omega}\right]_{Ne} = \left[\frac{d^2W}{d\Omega d\omega}\right]_{1e} \cdot \left(N + N(N-1)f(\omega)\right), \tag{27}$$

where $f(\omega) = |\int_{-\infty}^{+\infty} f(s)\exp(-i\omega s/c)ds|^2$ is the bunch form factor (BFF).[5] In a wide spread configuration the autocorrelation of the radiation is measured and the bunch length extracted. The BFF can be inferred from the autocorrelation function via the Wiener-Kitchine relation. The autocorrelation and the BFF do not include any phase information of the electic field, since it is lost in a power measurement. It can however be recoverd by means of the Kramers-Kronig relation, thus the longitudinal charge density can be reconstructed. In case of an asymmetric longitudinal bunch profile the method does not allow to determine which side of the distribution belongs to the head and which side belongs to the tail of the bunch. This information has to be gained by other means. At intermediate bunch length (i.e. $\sigma_s \simeq 100\,\mu$m) the low frequency cut-off of the detector (due to diffraction) results, in addition, to a loss of information in the low frequency region of the spectrum which needs to be extrapolated and introduces some ambiguity. A similar problem can occur for ultrashort bunch length, where the problem comes from the missing high frequency component (typically due to the cut-off of optical elements that compose the interferometer). In this case a new technique based on fluctuation measurements [36] is foreseen.
Instead of measuring the autocorrelation of the coherent radiation, the spectrum can directly be measured with a single shot polychromator such as designed by the Tokuhu Univ. team [37]. This measurements can directly provide the relevant information. First it provides a single shot spectrum from which the bunch length can be calculated, since the asymptotic expansion of the BFF at low frequencies is: $\lim_{\omega\to 0}[f(\omega)] \simeq 1 - \omega^2/c^2\sigma_s^2$. Secondly, the machine stability can be monitored by observing selected frequencies, since different types of jitter and drift generate typical signatures on the BFF.
In order to derive the BFF from the data of a macroparticle simulation the longitudinal charge density is written as a Klimontovich distribution:

$$S(t) = \frac{1}{N}\sum_{i=1}^{N}\delta(t - t_i), \tag{28}$$

[5] Transverse effects and the angular opening of the system should be taken into account.

for which the BFF simplifies to:

$$f(\omega) = \frac{1}{N^2}\left[\left(\sum_{i=1}^{N}\sin(\omega t_i)\right)^2 + \left(\sum_{i=1}^{N}\cos(\omega t_i)\right)^2\right]. \tag{29}$$

An example of the evolution of the BFF for phase shifts of the accelerating and the third harmonic section (compared to the nominal case) is presented in Fig. 39: Depending on the type of detector a sensitivity at the RF degree level can be expected.

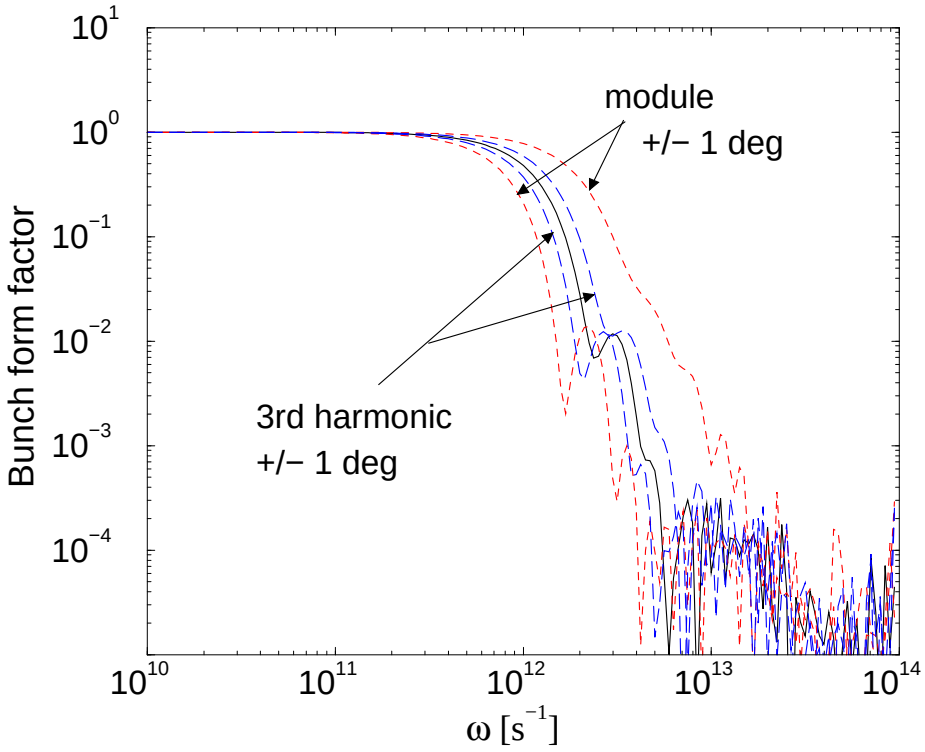

Figure 39: Sensitivity of the bunch form factor on phase offsets of the accelerating section and the third harmonic section. The solid line is the bunch form factor for the nominal settings.

4.3.4 Longitudinal transfer map

The longitudinal transfer map of a linac section can be measured with a technique, which can be viewed as a longitudinal difference orbit technique: The phase (or energy) of the beam upstream of the section is varied and the relative time of flight downstream the section is measured. This technique has been used in a DC-gun because the non-relativistic nature of the beam facilitates a time-of-flight measurement [32]. In an RF photoinjector this technique can be used to measure the longitudinal transfer map of the accelerating section, the 3^{rd} harmonic section and the first bunch compressor. The measurement allows to set up the operating phase of the first accelerating section and the third harmonic section.

Varying the photocathode laser launch time T_{in} and measuring the relative time-of-flight downstream of the compressor T_{out}, will provide information on the Taylor expansion of the longitudinal transfer map: $\partial s_{out}/\partial s_{in}$ ($s = cT$) and thus the compression rate between the photocathode and the bunch compressor exit. It provides therefore a tool to control the operation of the first bunch compressor.
Varying the gradient of the last cavity of the accelerator module gives information on the impact of the third harmonic section and quantifies if the distortions, at this position of the transport line, are removed as expected from simulations. Similarly to the previous case, information on the transfer map $\partial s_{out}/\partial \delta_{in}$ can be obtained.
Again both measurements provide quantitative information that can be compared to particle tracking and optics programs, but also qualitative information, which can be used by an operator to ensure the reproducibility of the settings. To perform the measurement, the variability of the photocathode laser phase and/or the variability of the gradient of the last cavity in the accelerating section (with a few Hz frequency, depending on the beam repetition rate) has to be realized.
A possible set-up would be to detect the TM_{010} waves excited in a pill-box cavity with resonant frequency of 1.3 GHz. The principle of a precise phase measurement is as follow: The RF signal $V_{rf}\sin(\omega t+\phi_{rf})$ coming from the cavity is mixed with a reference signal that can be shifted by means of a programmable phase shifter $V_0\sin(\omega t+\phi_0)$. The signal at the output, after removal of the high frequency, is $V_{out} = (V_{rf}V_0)/2\sin(\Delta\phi)$ where $\Delta\phi = \phi_{rf} - \phi_0$. The coefficient $(V_{rf}V_0)/2$ can be determined with a simple calibration procedure, that consists of varying the phase shifter and find the two zero-crossings. Note, that given a $\Delta\phi$ the amplitude of the output voltage is directly proportional to the beam induced signal V_{rf}. Based on the performance of a similar measurement scheme [32] a TOF resolution well below the required 1 ps is expected. In Fig. 41 the sensitivity of this technique to miss-settings of the accelerating and third harmonic section is illustrated. The measurement can be fitted to obtain quantitative information on the Taylor expansion of the longitudinal transfer map. For the simulations of Fig. 41 a 0.5 ps phase jitter on the input phase was superimposed; even with this jitter the sensitivity of the measurement is at the RF degree level. A first test of the TOF measurement is in preparation at the TTF.

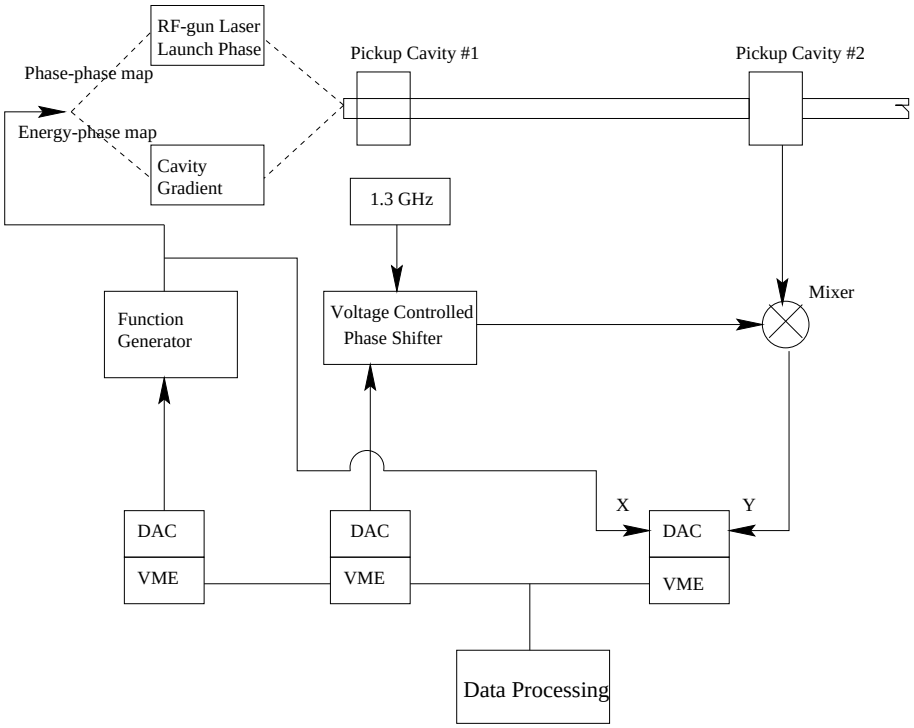

Figure 40: Block diagram of a longitudinal transfer map measurement electronics.

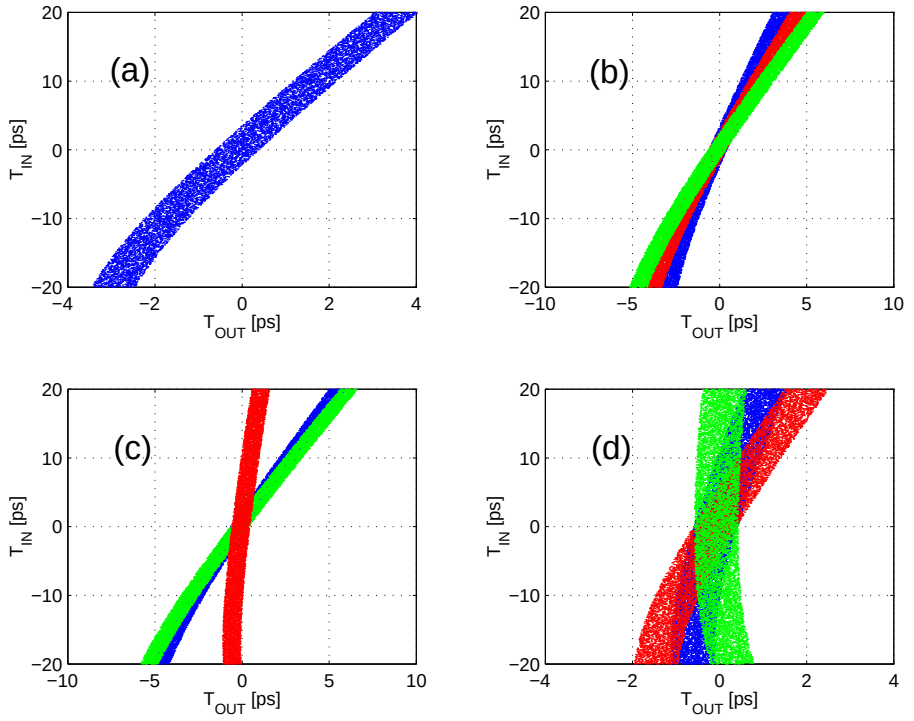

Figure 41: Simulation of the longitudinal transfer map measurement for different settings of the accelerating and third harmonic sections: (a) nominal set-up of the beam line, (b) effects of a phase drift of $+2°$ and $+4°$ of the third harmonic section, (c) effects of a phase drift of $\pm 2°$ of the accelerating section, (d) effects of a phase drift of $\pm 2°$ of the third harmonic section with the first accelerating section set up to satisfy the condition for maximum compression.

5 Conclusion and Future Directions

A photoinjector for the TESLA XFEL is proposed, the achieved beam parameters at the injector exit (including compression) are:

$$\begin{aligned} q &= 1\,\mathrm{nC} \\ \varepsilon_{x,y} &\simeq 0.9\,\mathrm{mrad\,mm} \\ \sigma_z &= 270\,\mu\mathrm{m} \\ \sigma_{E,uncorr} &= 93\,\mathrm{keV} \end{aligned}$$

Full tracking of the distribution along the complete TESLA linac up to the FEL undulators is in progress [12] and first results indicate that the achieved beam quality at the undulator entrance is within the specifications. An overview of the FEL-injector is presented in Fig. 42; the footprint of the beam line elements is about $45 \cdot 2\,\mathrm{m}^2$. An important feature of the present design is the use of a third order radio-frequency section to linearize the longitudinal phase space. This technique is also planned to be used in the TTF FEL User Facility and an R & D program to develop 3.9 GHz superconducting cavities based on a scaled TESLA 1.3 GHz cavity is going to be started. On the experimental side, the injector test facility under construction at DESY-Zeuthen will allow to tests some of the concepts presented in this note. Other tests will be performed at the TTF and at the A0 injector [38] at FNAL.

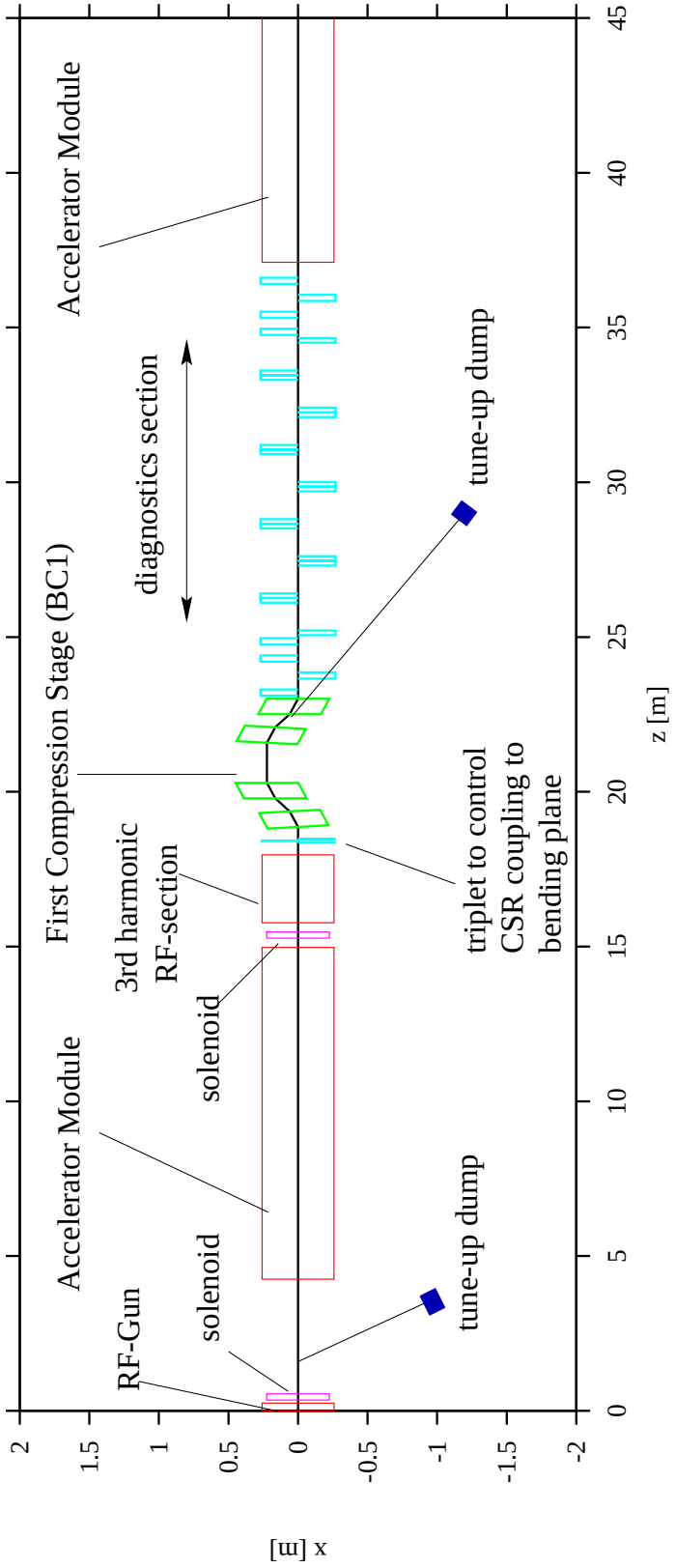

Figure 42: Overview of the TESLA XFEL injector.

A Comparison of ASTRA and HOMDYN Results

Figs 43 to 46 show a comparison between ASTRA and HOMDYN results. The evolution of the beam parameters along the beam line shows besides a general agreement small differences. The phase space snap shots indicate a non linear distortion of the transverse phase space as calculated with ASTRA. A detailed analysis shows, that this distortion is due to non linear space charge force close to the cathode. In the first phase space plots at z =0.39 m and z =2.51 m the distortion is covered by the large correlated emittance contributions and can only be resolved after removal of this correlations.

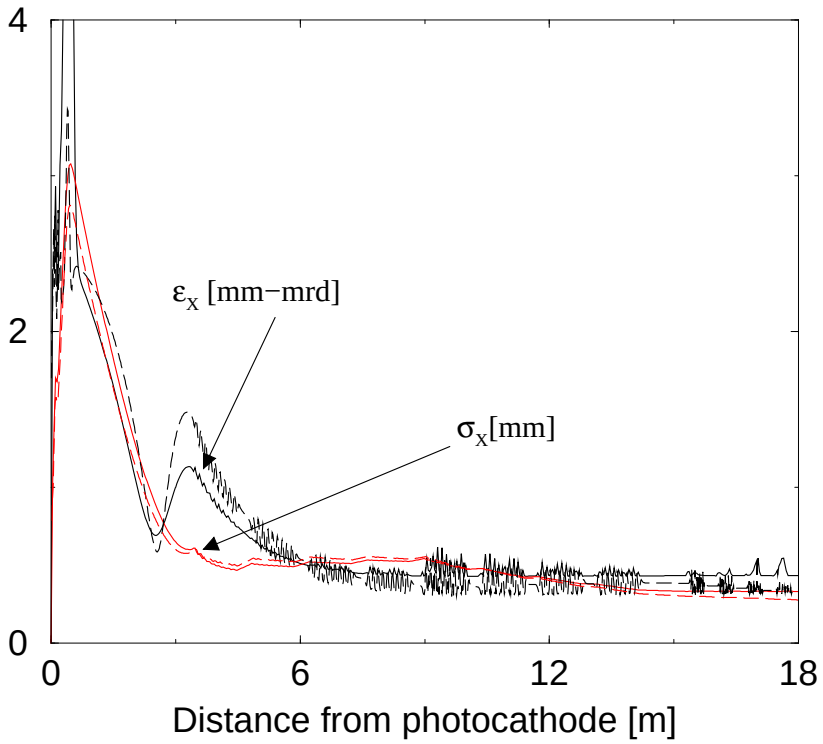

Figure 43: Transverse beam parameter evolution along the beam line from the photocathode up to the exit of the third harmonic section calculated with ASTRA (solid lines) and HOMDYN (dashed lines).

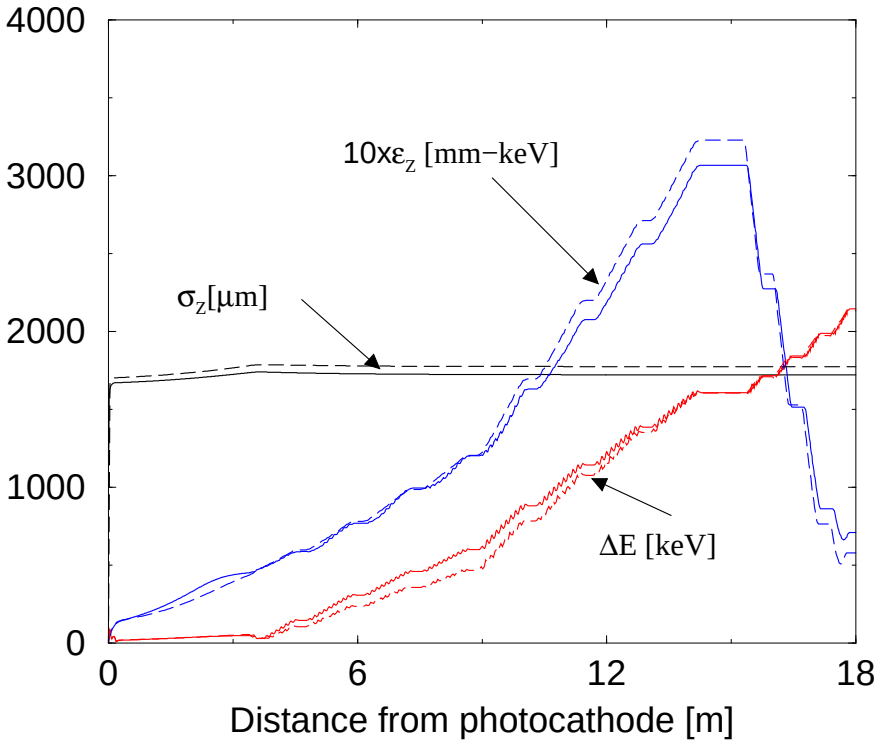

Figure 44: Longitudinal beam parameter evolution along the beam line from the photocathode up to the exit of the third harmonic section calculated with ASTRA (solid lines) and HOMDYN (dashed lines).

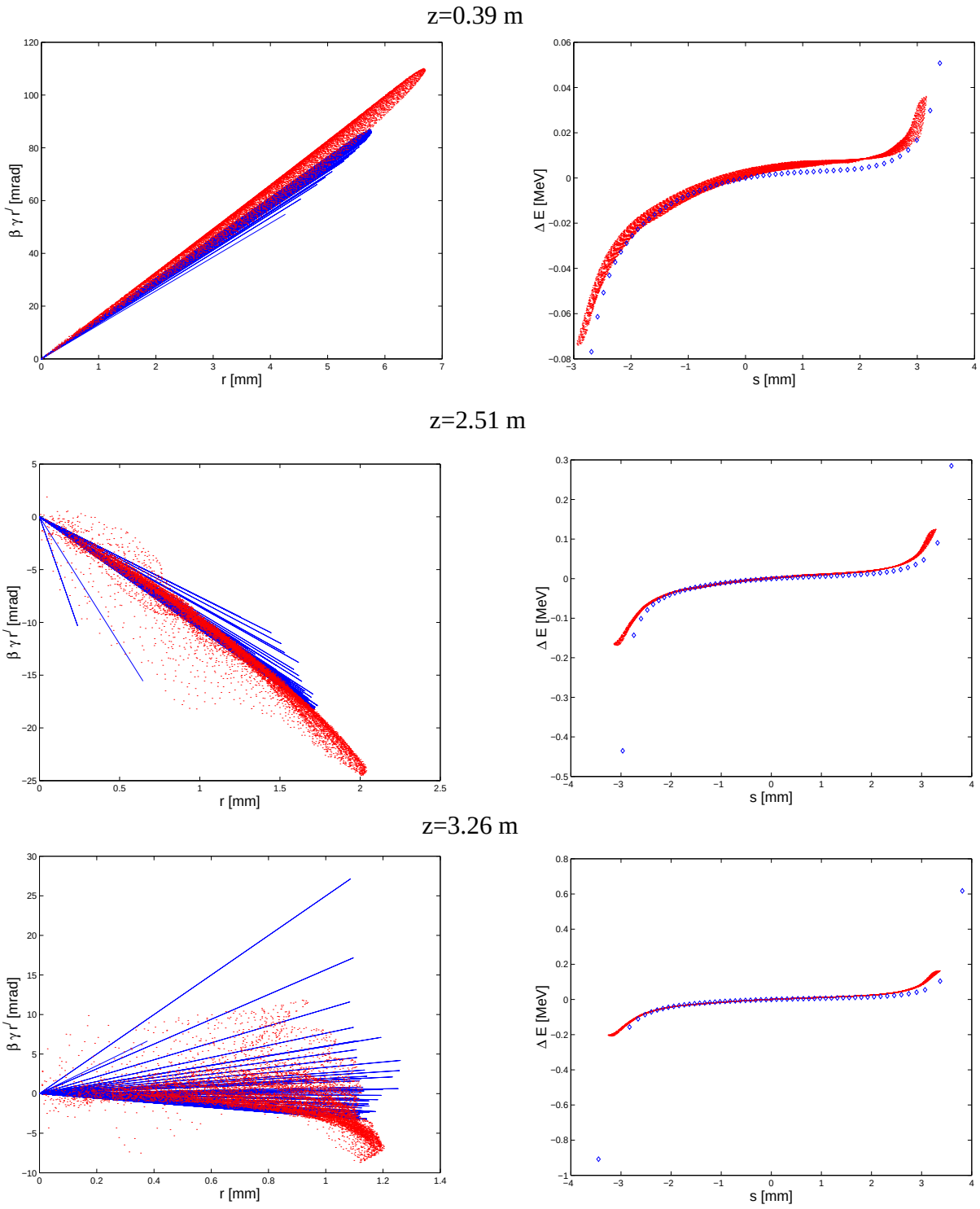

Figure 45: Transverse (left) and longitudinal (right) phase space plots at various locations along the beam line. The red dots are macroparticles from ASTRA the blue lines and diamonds indicate the slices of HOMDYN.

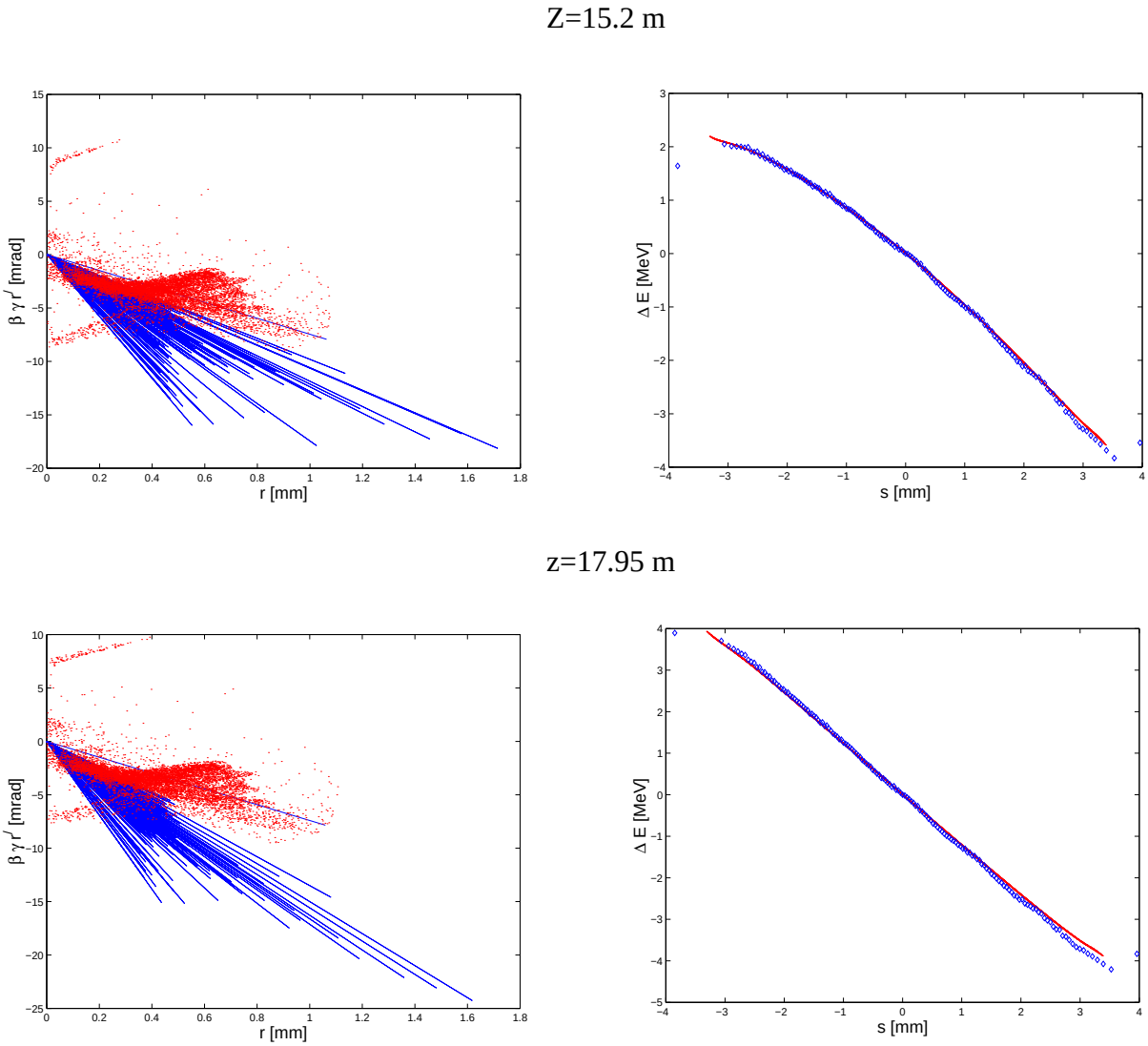

Figure 46: Transverse (left) and longitudinal (right) phase space plots at various locations along the beam line. The red dots are macroparticles from ASTRA the blue lines and diamonds indicate the slices of HOMDYN.

References

[1] Ferrario M., Serafini L.,"Multi-bunch dynamics in RF photoinjectors through an envelope equation approach" in proceeding of EPAC'98, pp.1271-1273 (1998)

[2] Flöttmann K, *Astra User Manual*,

`http://www.desy.de/~mpyflo/Astra_dokumentation/`

[3] Borland M., *Elegant User Manual*,

`http://www.aps.anl.gov/asd/oag/manuals/elegant_ver14.1`

[4] Dohlus M., Kabel A., and Limberg T., "Numerical calculation ofcoherent synchrotron radiation effects using TraFiC-4" *Nucl. Instr. Meth.* **A445**, pp. 338-342 (2000)

[5] Will I., Liero A., Merins D., Sander W., "Feedback-stabilized Nd:YLF amplifier system for generation of picosecond pulse trains of an exactly rectangular envelope", *IEEE Journ. Quant. Electronics*, **34** pp. 2020-2028 (1998)

[6] Sertore D., Schreiber S., Stephan F., Flöttmann F, Zapfe K., and Michelato P.,"First operation of Cesium Telluride photocathodes in the TTF injector RF gun", *Nucl. Meth. Instr.* **A 445**, pp. 422-426 (2000)

[7] Stephan F. et al., "Photo Injector Test Facility under Construction at DESY Zeuthen", Proc. Free Electron Laser Conf., 13-18 Aug. 2000, Durham, North Carolina.

[8] Dwersteg D., Flöttmann K., Sektowicz J., Stolzenburg Ch., "RF gun design for the TESLA VUV Free Electron Laser", *Nucl. Instr. Meth.* **A 393**, pp. 93-95 (1997)

[9] Flöttmann K, "Note on the thermal emittance of electrons emitted by Cesium Telluride photocathode", TESLA-FEL **97-01** (1997)

[10] Travier C., "Le canon HF de CANDELA", Thèse de doctorat Université Paris-Sud (1996)

[11] Private communication, Conde M., ANL.

[12] Piot Ph., Limberg T., "Integrated Modeling of the TESLA X-FEL beam line", to be presented at PAC'01

[13] Limberg T., Piot Ph., "Optics Optimization for Multistage Bunch Compression", to be presented at PAC'01

[14] Smith T. I., "Intense low emittance linac beams for free-electron lasers", *proc linear acc. conf.'84* SLAC report **303**, pp. 421-425 (1986);

Dowell D., et. al, "The BOEING photocathode accelerator magnetic compression and energy recovery experiment", *Nucl. Instr. Meth.* **A375**, pp. 108-111 (1996);

Piot Ph., Flöttmann K. Limberg T., TESLA-FEL **01-06** (2001)

[15] Carlsten B.E., "New photoelectric injector design for the Los Alamos National Laboratory XUV FEL accelerator", *Nucl. Instr. Meth.* , **A285** pp. 313-319 (1989)

[16] Serafini L., "Overview on production and beam dynamics of high brightness beams", **AIP** conference proceedings CP395, *Nonlinear and Collective Phenomena in Beam Physics* edited by S. Cattopadhyay, M. Cornacchia, and C. Pellegrini (1997)

[17] Qiu X., et al. "Demonstration of Emittance compensation through the measurement of the slice emittance of a 10-ps electron bunch", *Phy. Rev. Lett.* vol. **76**, num. 20, pp. 3723-3726 (1996)

[18] Poisson code available from Los Alamos (NM) National Lab.

[19] Aune B., et al., "Superconducting TESLA cavities", *Phys. Rev. ST Accel. Beams* **3**, 092001 (2000)

[20] Zhao Q., et al., "The Photoinjector Test Stand in Zeuthen", to be presented at PAC'01 conference

[21] Ferrario M. et al.,"HOMDYN study for the LCLS RF photo-injector", LNF-00/004(P) and SLAC-PUB 9400 , to be published in the 2nd ICFA Advanced Accelerator Workshop held Nov 9-12 1999 in Los Angeles CA USA

[22] *Linac Coherent Light Source (LCLS) Design Study Report*, reports **SLAC-R**-521 and UC-414, Stanford (April 1998)

[23] This is similar to the scheme proposed for NLC (Emma P., "A skew Correction and Diagnostics Section for Linear Collider", unpublished) see also p. 758 in *Conceptual Design of a 500 GeV Linear Collider with Integrated X-ray laser Facility*, DESY-97-048 (1997)

[24] Brinkmann R., private communication (Nov. 2000)

[25] E.L. Saldin, E. Schneidmiller, M. Yurkov, "On the coherent radiation of an electron bunch moving in an arc of a circle", *Nucl. Instr. Meth.* **A398** p. 373 (1997)

[26] Warnock R.L. and Morton P., *proceedings of PAC'91*, pp. 1824-1826 (IEEE, Piscataway, NJ, 1991)

Murphy J.B., Krinsky S., and Gluckstern R. L., "Longitudinal wakefield for an electron moving on a circular orbit", *Particle Accelerators* **57**, pp. 9-64 (1997)

[27] von Walter G., "Entwicklung und Optimierung einer Regelung für die Hochfrequenz-Photoelektronenquellen am TTF-Linerabeschleuniger" RWTH Aachen, PITHA 99/34, 1999.

[28] This is a generalized form of a similar scheme proposed elsewhere, private communication from Douglas D.R., Jefferson Lab (1999)

[29] Denard J-.C., Piot Ph., K. Capek, E. Feldl," High Power Beam Profile Monitor with Optical Transition Radiation", *proceedings of PAC'97* Vancouver, pp. 2198-2200 (1997)

[30] Graves W. S., Johnson E. D., O'Shea P. G., "A High Resolution Electron Beam Profile Monitor", *Proc. of the PAC'97* Vancouver, pp. 1993-1995 (1997)

[31] Catravas P., Leemans W.P., et al. "Beam profile measurement at 30 GeV using optical transition radiation", *proceedings of PAC'99* New-York City (1999)

[32] Krafft G.A., "Correcting of M_{56} and T_{566}" AIP conf. proceedings **367**, pp 46-55 (1995), Piot Ph., Douglas D.R., Krafft G.A. "Study of energy compression scheme to energy recover an electron beam in presence of an FEL interaction", *proceedings of EPAC 2000* (Vienna), pp. 1543-1545 (2000)

[33] Hamamatsu Corp. Japan

[34] Useka M., Ueda T., Kozawa T., Kobayashi T., "Precise measurement of subpicosecond electron single bunch by femtosecond streak camera", *Nucl. Instr. Meth.* , **A406** pp. 371-379 (1998)

[35] Wang D.X., Krafft G.A., Sinclair C.K., *Phy. Rev.* **E57**, p. 2293 (1998); the method has been extended to the case of beam with significant energy spread in Piot P., Krafft G.A."Bunch length measurement with back-phasing technique for non emittance-dominated beam with significant intrinsic energy spread". JLab-TN-98-029.

[36] Krzywinsky J., Saldin E.L., Schneidmiller E.A., Yurkov M.V., "A new method for ultrashort electron pulse-shape measurement using synchrotron radiation from bending magnet", TESLA-FEL **97-03** (1997); Catravas P., Leeman W.P., et al. "Measurement of electron-beam bunch length and emittance using shot-noise-driven fluctuation in incoherent radiation" *Phys. Rev. Lett.*, **82** num. 26, pp. 5261-5264 (1999)

[37] Kondo Y., "Ten Channel grating polychromator for far-infrared transient spectroscopy" private communication of Dec 26th 1996. The device has been used for results reported e.g. in Nakazato T. et al, "Observation of coherent synchrotron radiation", *Phys. Rev. Lett.* **63**, p. 1245 (1989)

[38] Carneiro J.-P., et al., "First reults of the FERMILAB high-brightness RF photoinjector", *proceedings of PAC'99* New-York City, pp. 2027-2029 (1999)